Petroleum Science 23 (2026) 7561–7577

Contents lists available at ScienceDirect

Petroleum Science

journal homepage: www.keaipublishing.com/en/journals/petroleum-science

Original Paper

Large-scale 3D experimental study on in-situ pyrolysis of tar-rich coal (II): heat transfer behavior and migration mechanisms under convective heating

Yan-Wei Li [a,b,c,d], Chao-Fan Zhu [a,b,c,d,**], Yi-Jian Zeng [a,b,c,d], Han Tian [a,b,c,d], Tian-Le Zhang [a,b,c,d], Wei Guo [a,b,c,d,*]

[a] State Key Laboratory of Deep Earth Exploration and Imaging, College of Construction Engineering, Jilin University, Changchun, 130026, Jilin, China
[b] National-Local Joint Engineering Laboratory of In-situ Conversion, Drilling and Exploitation Technology for Oil Shale, Jilin University, Changchun, 130021, Jilin, China
[c] Provincial and Ministerial Co-construction of Collaborative Innovation Center for Shale Oil & Gas Exploration and Development, Jilin University, Changchun, 130021, Jilin, China
[d] Key Lab of Ministry of Natural Resources for Drilling and Exploitation Technology in Complex Conditions, Jilin University, Changchun, 130021, Jilin, China

ARTICLE INFO

Article history:
Received 3 February 2026
Received in revised form
18 April 2026
Accepted 6 July 2026
Available online 20 July 2026

Edited by Min Li

Keywords:
Tar-rich coal
Convective heating
In-situ pyrolysis
Pore structure
Ordos Basin

ABSTRACT

Convective heating is a key technology for in-situ pyrolysis of tar-rich coal. However, research on temperature and pressure characteristics, oil and gas generation mechanisms, and reaction zone characteristics under high-pressure, large-scale conditions remains limited. This study used a self-developed high-temperature, high-pressure in situ pyrolysis apparatus to conduct convective heating experiments on tar-rich coal from the eastern Ordos Basin. Temperature and pressure evolution was analyzed, while the oil and gas products and post-pyrolysis rock samples were characterized using GC/GC-MS, XRD, and CT analyses. The results were then compared with those obtained under conductive heating. The results indicate a significant enhancement in both pyrolysis efficiency and spatial sweep. The average heating rate reached 2.24 °C/h, which was 3.2 times that under conductive heating; meanwhile, the temperature-field homogenization rate was 5.15 times that under conductive heating, and the effective intense-pyrolysis volume fraction increased from 7.7% to 23.6%. Driven by strong dynamic carryover, oil and gas recovery was significantly improved. Oil production began 203 h earlier than under conductive heating. The cumulative oil and gas yields reached 24.48% and 92.42%, respectively, which were 12.42 times and 3.27 times the corresponding values under conductive heating. Reservoir flow conductivity was maintained, with an average permeability of 42.90 mD, 7.96 times the corresponding value under conductive heating. The local maximum porosity after pyrolysis reached 30.1%, and the area with porosity exceeding 14% accounted for 60%. The upward migration of low-density oil and gas products was more pronounced. Therefore, a horizontal well configuration with middle-lower injection and dual top-bottom production is recommended to maximize recovery efficiency. This study establishes a theoretical and experimental foundation for in-situ pyrolysis of tar-rich coal under convective heating.

© 2026 Publishing services by Elsevier B.V. on behalf of KeAi Communications Co. Ltd. This is an open access article under the CC BY-NC-ND license (http://creativecommons.org/licenses/by-nc-nd/4.0/).

1. Introduction

Coal is an important part of global energy (Wang et al., 2025). Tar-rich coal refers to coal resources with a tar yield of 7.0%–12.0%; because it is rich in organic matter that can be converted into oil and gas, it is regarded as a comprehensive resource integrating coal, oil, and gas attributes, and has become an emerging field of energy development (Tian et al.,

* Corresponding author.
** Corresponding author.
E-mail addresses: chaofan_zhu@jlu.edu.cn (C.-F. Zhu), guowei6981@jlu.edu.cn (W. Guo).

Peer review under the responsibility of China University of Petroleum (Beijing).

https://doi.org/10.1016/j.petsci.2026.07.010
1995-8226/© 2026 Publishing services by Elsevier B.V. on behalf of KeAi Communications Co. Ltd. This is an open access article under the CC BY-NC-ND license (http://creativecommons.org/licenses/by-nc-nd/4.0/).

2016). The traditional way of using tar-rich coal is to mine and transport it to the surface, then extract oil and gas through retorting furnace pyrolysis, but this conversion technology causes severe environmental pollution (Ju et al., 2021). To reduce environmental damage, underground in-situ pyrolysis technology was proposed. This technology injects heat into the coal seam to crack the solid organic matter, producing liquid and gaseous resources that are subsequently recovered at the surface for processing (Li et al., 2023). Underground in-situ pyrolysis is green and low-carbon, can support the green development of the coal industry, and is a research hotspot in current tar-rich coal fields (Xu et al., 2023a).

A critical challenge in underground in-situ pyrolysis of tar-rich coal is achieving efficient heat injection. According to heating principles, it is mainly divided into four types: conduction heating (Maloney et al., 1999), convection heating (Smart et al., 2010), radiation heating (Shamsi et al., 2021), and reaction heating (Guo et al., 2022). Specifically, convective heating technology injects a high-temperature heat-carrying fluid into the coal seam, using direct heat exchange between the fluid and the coal matrix to accelerate heat transfer and thereby promote oil and gas release. This technique has garnered significant attention in recent years due to its distinct advantages, including uniform heating, high heat transfer efficiency, and favorable conditions for hydrocarbon production (Kang et al., 2020a; Shui et al., 2026; Suo et al., 2024a). Our research group employed a sequential method involving convective preheating with high-temperature nitrogen followed by the injection of ambient air to induce oxidative heat generation. This approach was successfully applied to the in-situ pyrolysis of oil shale in the Nong'an and Fuyu regions of China (Guo et al., 2023b; Zhu et al., 2025a).

Existing research on convective heating for in-situ pyrolysis of tar-rich coal has primarily relied on laboratory-scale experiments, focusing on selecting heat-carrier fluids and their underlying mechanisms. Various heat-carrier fluids have been proposed, including N_2 (Zhu et al., 2022), steam (Kang et al., 2020b; Wang et al., 2021), CO_2 (Gao et al., 2013), supercritical CO_2 (Zhao et al., 2020), and near-critical water (Deng et al., 2011). Among these, N_2 serves as an inert medium that effectively prevents oxidation reactions, yielding high-quality hydrocarbons and maintaining a high semi-coke yield (Zhao et al., 2012). Steam enhances coal gasification and accelerates organic matter cracking, thereby enriching H_2 and CO concentrations while inhibiting the formation of oxygenated compounds (Chang et al., 2024; Yang et al., 2021). A CO_2 atmosphere promotes coal gasification, reducing semi-coke yield while increasing pyrolysis gas and tar production (Gao et al., 2013). Supercritical CO_2 exhibits superior heat and mass transfer properties, along with substantial dissolution and extraction capabilities, resulting in a recovery rate significantly higher than that of nitrogen (Zhao et al., 2020). Near-critical water, characterized by high solubility, not only promotes the cracking of macromolecules to enhance hydrocarbon yield but also increases the hydrogen content in gaseous products via hydrogenation reactions (Deng et al., 2011). In addition to the heat-carrier fluid, temperature (Suo et al., 2024b), pressure (Tian et al., 2025; Zhang et al., 2024), and flow rate (Liu et al., 2011) constitute critical parameters influencing pyrolysis efficiency. The primary thermal decomposition temperature range for tar-rich coal lies between 400 and 550 °C; within this range, elevated temperatures accelerate the cracking of organic matter, thereby enhancing hydrocarbon release (Xu et al., 2024). However, excessively high temperatures induce secondary cracking reactions, resulting in a reduction in tar yield and a concurrent increase in gas yield (Qu et al., 2024). The flow rate directly dictates heat transfer efficiency (Xu et al., 2019): while high flow rates accelerate heat transfer, they are prone to causing thermal heterogeneity, whereas excessively low flow rates result in insufficient heat supply (Yang et al., 2023). Pressure is intrinsically linked to temperature variations; high-pressure environments significantly inhibit volatile yield and prolong the residence time of tar within the coal seam, thereby intensifying secondary reactions that lower tar conversion rates and increase coke production (Chen et al., 2025). Although existing laboratory experiments have elucidated the effects of various heat-carrier fluids and physical parameters on convective heating, research concerning the dynamic evolution of multi-field parameters during the in-situ pyrolysis of tar-rich coal remains insufficient. Practical in-situ pyrolysis engineering typically operates within complex environments characterized by high pressure, large scales, and long-term multi-field coupling; however, current studies are largely confined to small-scale laboratory settings or idealized conditions, leaving a gap in the systematic understanding of temperature and pressure characteristics, hydrocarbon generation mechanisms, and reaction zone features under these realistic high-pressure, large-scale conditions. To address this gap, Part I of this series systematically investigated the in-situ pyrolysis of tar-rich coal under conductive heating using a large-scale 3D experimental apparatus. While Part I established a baseline for temperature evolution and product characteristics, it also revealed severe engineering bottlenecks: an extremely low heat transfer efficiency and critical pore blockage caused by the condensation of heavy components in low-temperature zones, which restricted the oil yield to a mere 1.97% (Li et al., 2026).

To fundamentally overcome these limitations, this paper (Part II) shifts the research paradigm to convective heating. Focusing on tar-rich coal from the eastern Ordos Basin, China, we upgraded the original conductive heating system to develop a novel, high-temperature, high-pressure in-situ convective experimental apparatus. The investigation examines the evolution of temperature and pressure, the mechanisms of product generation, and reaction zone characteristics during the in-situ conversion process. Gas chromatography (GC) and gas chromatography-mass spectrometry (GC-MS) were employed to analyze the components of oil and gas products, while rock pyrolysis, X-ray diffraction (XRD), and computed tomography (CT) scanning were integrated to characterize the organic properties, inorganic mineral evolution, and pore structure of the resulting semi-coke. Furthermore, the results were compared with data from conductive heating experiments. This study establishes a theoretical and experimental foundation for in-situ pyrolysis of tar-rich coal.

2. Materials and methods

2.1. Materials

The tar-rich coal samples were collected from a 12.96-m-thick coal seam at a burial depth of approximately 1500 m in the eastern Ordos Basin, China (Wang et al., 2019). The basic properties of the samples are listed in Table 1. Low-temperature carbonization tests conducted at 550 °C under an N_2 atmosphere revealed a tar yield of 9.11% and a gas yield of 5.75% for the raw samples. Rock-Eval pyrolysis analysis indicated a free hydrocarbon (S1) content of 8.29 mg/g, demonstrating the presence of abundant free hydrocarbons. Meanwhile, the pyrolysis hydrocarbon potential (S2) reached 119.72 mg/g, confirming the substantial hydrocarbon generation potential of this tar-rich coal(Wang et al., 2025). Mineralogical analysis identified kaolinite and tobelite as the dominant inorganic phases, accompanied by minor occurrences of calcite and pyrite.

Table 1
Basic physical properties of original tar-rich coal.

Fischer assay analysis, wt% (ad)		Rock-Eval pyrolysis		Inorganic minerals, %	
Tar	9.11	S1, mg/g	8.29	Kaolinite	69.58
Gas	5.75	S2, mg/g	119.72	Calcite	9.10
Water	3.03			Pyrite	1.21
Char	82.11			Tobelite	20.11

Note: ad, air-dried basis.

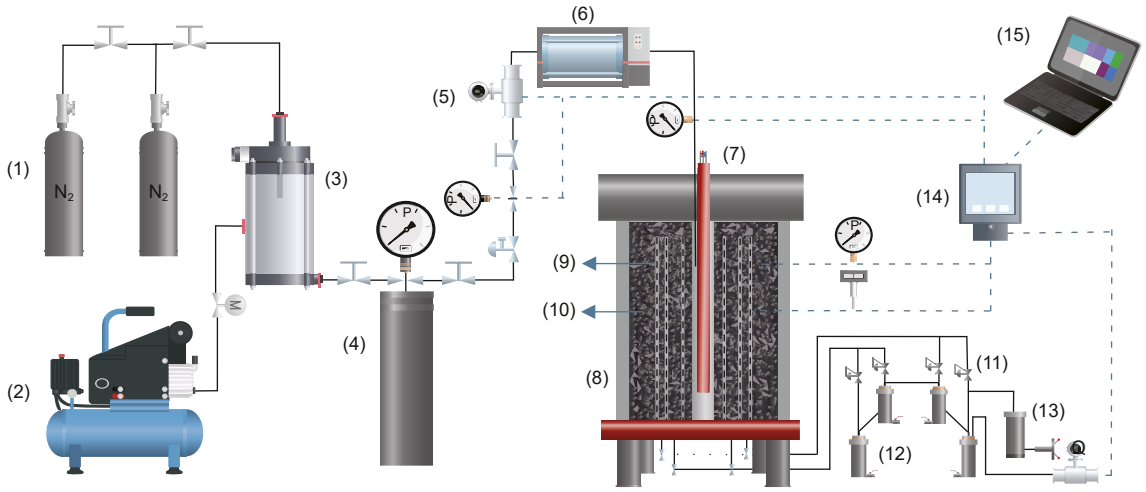


Fig. 1. Schematic diagram of the in-situ convective pyrolysis of tar-rich coal: (1) gas cylinder; (2) air compressor; (3) booster pump; (4) buffer tank; (5) gas flow meter; (6) preheater; (7) heater; (8) reactor; (9) coal sample; (10) temperature sensor; (11) back pressure valve; (12) product collection tank; (13) hand pump; (14) paperless recorder; (15) data acquisition.

2.2. Experimental apparatus and procedure for in-situ pyrolysis

This study investigates the in-situ pyrolysis of tar-rich coal using a self-developed experimental platform. Fig. 1 presents the schematic diagram of convective in-situ pyrolysis of tar-rich coal. The experimental apparatus comprises four primary subsystems: the injection system, the high-temperature and high-pressure reaction system, the product collection and measurement system, and the data acquisition and control system. The high-temperature, high-pressure reactor has an inner diameter of 710 mm and a height of 1000 mm. Due to the large scale of the experimental setup, strict full-scale parallel repeat experiments were not feasible. To ensure the reliability of the results, an internal consistency verification strategy was adopted. Specifically, redundant sensors were symmetrically arranged at identical radial and vertical positions to provide spatially repeated measurements, thereby validating the stability of the experimental process and the consistency of the results. Four product outlets are located at the bottom of the reactor, uniformly distributed along a circumference with a radius of 250 mm from the center. Key internal components of the reactor include a heater, a heating tube, and a central tube serving as the gas inlet channel. The heating tube and the heater are positioned at 100 mm and 200 mm above the reactor bottom, respectively. To monitor the reactor's internal temperature field, 12 stainless steel thermowells were installed at radial distances of 125, 250, and 320 mm from the central axis along four orthogonal azimuthal directions. A total of 60 temperature sensors were deployed within the reactor. These sensors were distributed axially at heights of 100, 300, 500, 700, and 900 mm from the reactor bottom, and radially at 125, 250, and 320 mm across four orthogonal azimuthal directions (at 90° intervals). Additionally, the reactor exterior is equipped with trace heaters and insulation wool to compensate for heat loss, while one inlet pressure sensor, one reactor body pressure sensor, and four outlet pressure sensors were installed on the reactor top. System pressure was monitored using high-frequency pressure transducers with a range of 25 MPa and an accuracy of ±0.1% of full scale. A PID system maintained the injection temperature within ±1 °C, while temperature measurements were taken with K-type thermocouples. Additionally, the outlet gas flow rate was measured using a wet gas meter. To simplify the geometric model for analysis, a half-sectional representation of the reactor was used in the subsequent analysis, as shown in Fig. 2.

The experimental procedure for convective heating comprises three primary stages, as illustrated in Fig. 3: core preparation, equipment assembly, and data collection. During the core preparation stage, tar-rich coal samples were pulverized to a particle size finer than 120 mesh. A central tube and 12 stainless steel thermowells were installed within the reactor, and the coal sample was reconstituted using a layered compaction technique (Xu et al., 2023b). Specifically, 10 kg of powder was loaded per layer and compressed at 40 MPa for 10 min, resulting in a cylindrical core with a diameter of 710 mm and a height of 1000 mm after repeated operations. In the equipment assembly stage, the reactor lid, preheater, internal heater, trace heaters, 60 temperature sensors, and 6 pressure sensors were installed sequentially, followed by connection of the pipelines, gas booster system, and product collection unit. Subsequently, airtightness inspections and permeability tests were conducted on all heating components and the overall assembly, revealing an initial permeability of 5.12 mD for the compacted coal sample. During data collection, temperature and pressure data from the heater, preheater, trace heaters, and various measurement points were recorded in real time. Oil and gas products at the outlet were sampled and collected at 2–4 h intervals. Upon completion of the experiment, coring analysis was performed on the post-reaction coal samples. Throughout the

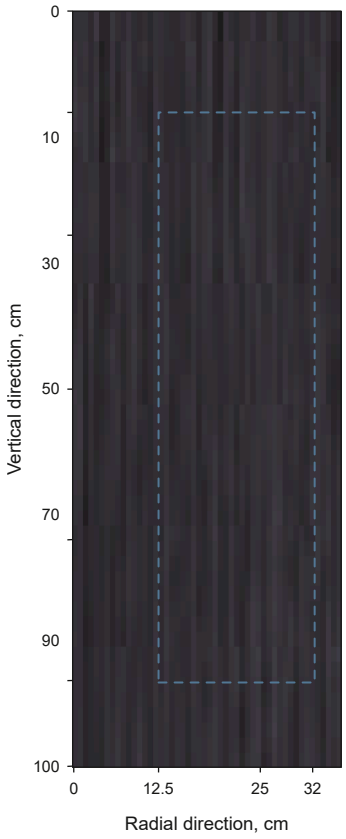


Fig. 2. Half-sectional view of the reactor.

convective experiment, the reactor pressure was maintained at 15 MPa, the heater power density was set to 3 kW/m, and the temperatures of both the heater and preheater were controlled at 500 °C. The average gas injection flow rate was regulated at 300 L/min. The back pressure was regulated to establish a production pressure differential of 1–2 MPa, thereby simulating the in-situ pyrolysis process.

2.3. Analytical methods

The chemical composition of the oil products was analyzed using an Agilent 7890A gas chromatograph coupled with an Agilent 5975N mass spectrometer (GC-MS). An HP-5MS capillary column (30 m × 0.32 mm) was employed, with an oven temperature program consisting of a 5-min hold at 50 °C, followed by a ramp to 280 °C at 10 °C/min, and a final hold of 12 min. Mass spectrometry was performed at 70 eV, and chemical components were identified using the NIST 2.0 library. Gaseous products were analyzed using an Agilent 7890B gas chromatograph equipped with a flame ionization detector (FID) for detecting C_1-C_6 hydrocarbons. A thermal conductivity detector (TCD1) fitted with a HayeSep A column was utilized to detect inorganic gases, including CO_2, CO, and N_2. A second thermal conductivity detector (TCD2), equipped with a 5 Å molecular sieve column, was explicitly dedicated to H_2 detection. Data collection and analysis were performed using Agilent OpenLab software; because nitrogen served as the carrier gas during pyrolysis, it was excluded from subsequent normalization calculations of gas composition. The properties of the semi-coke were characterized via Rock-Eval pyrolysis, XRD, and CT; organic parameters were evaluated using an OG-2000VA analyzer, for which samples were ground to 200 mesh with a sample mass of 10 mg. Parameters S0, S1, and S2 were obtained using programmed-temperature heating and FID detection. The mineralogical composition of the semi-coke was determined using an X'Pert PRO X-ray diffractometer with Cu Kα radiation, operated at a maximum voltage of 60 kV, a maximum current of 55 mA, and a maximum output power of 3 kW. The goniometer is a sample-holding type, and the 2θ angle range is 1° to 160°. Qualitative and quantitative phase analyses were performed based on diffraction peak intensities and the PDF-2 database. The pore structure of the semi-coke was characterized using a Nano Voxel 5000 Micro-CT system with a voxel size of 500 nm and a nominal spatial resolution of 200 nm; data were acquired via spiral scanning and reconstructed using Avizo software (Zhu et al., 2025b).

3. Results and discussion

3.1. Temperature and pressure characteristics

Figs. 4 and 5 show the temperature and pressure variation curves during convective heating. The evolutions of temperature and pressure exhibited a clear coupling relationship. As shown in Fig. 4(a), at a radial distance of 12.5 cm, the sample was rapidly heated during 0–46 h, with an average heating rate of 9.87 °C/h, and the temperature at 30 cm height reached 586.13 °C at 46 h. This phenomenon is likely attributed to the exothermic polycondensation reactions of coal and local heat accumulation (Hefta and Schobert, 1986; Wang et al., 2024). Meanwhile, the pressure difference between the inlet and outlet remained relatively small at approximately 1 MPa (Fig. 5), indicating that the system was mainly in the preheating stage and that the pressure response was primarily governed by the establishment of the internal flow field and fluid redistribution rather than by large-scale gas generation.

As heating proceeded, the near-well region gradually entered the active pyrolysis stage. After reaching its first peak at 46 h, the temperature at 12.5 cm decreased from 46 to 70 h, with an average cooling rate of −2.47 °C/h, suggesting outward heat transfer from the high-temperature core and substantial thermal conversion of local organic matter. In contrast, the temperatures at 25 cm and 32 cm continued to rise (Fig. 4(b) and (c)), indicating progressive outward propagation of the thermal front. Correspondingly, the system pressure increased significantly, suggesting that the pressure buildup in this stage was mainly driven by intensified pyrolysis and the large-scale release of volatiles and pyrolysis gases.

After 70 h, although the booster system failed, pyrolysis continued to advance. The delayed temperature peaks at 25 and 32 cm indicate that the active pyrolysis zone further expanded outward and that the distal region gradually entered the effective pyrolysis temperature range. At the same time, the temperature difference between 25 and 32 cm gradually decreased, reflecting progressive homogenization of the radial temperature field. Notably, the pressure did not vary monotonically with temperature but showed obvious fluctuations, especially during 70–93 h. This suggests that the pressure response was controlled not only by continuous gas generation but also by the dynamic adjustment of internal transport pathways associated with pore/fracture development and the migration of gaseous and condensable products.

During 93–147 h, the system entered a relatively stable slow-pyrolysis stage. The overall temperature field became more homogeneous, and the temperatures at different radial positions tended to converge. Although partial outlet blockage occurred, the pressure field still showed a generally consistent evolutionary



Fig. 3. Experimental procedure for the in-situ convective pyrolysis of tar-rich coal.

trend, and the average production pressure differential increased to 3.5 MPa, indicating that the late-stage pressure behavior was affected by residual pyrolysis, product migration, and local flow restriction.

Overall, the high-temperature fluid acted as an efficient heat carrier during convective heating, resulting in an overall average heating rate of 2.24 °C/h**.** Although the outer region exhibited a delayed thermal response, the radial temperature difference gradually decreased over time, leading to a more homogeneous temperature field and thereby favoring more efficient and spatially extensive pyrolysis conversion. Meanwhile, the accelerated heating process and enhanced fluid migration also intensified the internal pressure dynamics, with an average pressure differential of 1.31 MPa.

Fig. 6 shows the cloud map of the temperature field variation during convective heating. The data were processed using the Renka-Cline gridding interpolation algorithm implemented in Origin software (Renka et al., 1984). At 30 h, the temperature in the 12.5–30 region reached 433.1 °C, while the minimum temperature at the upper periphery was 107.35 °C. By 46 h, the temperature near the top center exceeded 542 °C, peaking at 586.13 °C, whereas the minimum temperature at the upper periphery remained at 121.83 °C. At this stage, heat was transferred uniformly upward via the fluid medium, intensifying thermal gradients across different locations. At 70 h, heat from the upper central region propagated further radially and downward; the local maximum temperature decreased to 507.58 °C, indicating that organic matter in this zone had undergone pyrolysis, while the minimum temperature at the upper periphery rose to 198.35 °C. By 93 h, the temperature near the center declined further; the maximum temperature in the top 12.5–10 region was 472.98 °C, and the temperature in the 32–30 region exceeded 429 °C, confirming that heat had effectively reached the upper boundaries. Simultaneously, the temperature in the 32–70 region exceeded 368 °C, indicating heat transfer to the bottom boundary. At 134 h, the temperature in the middle and upper sections of the reactor decreased to approximately 368 °C; overall, a large area of cooling was observed, indicating that pyrolysis of organic matter was still in progress. By 147 h, compared to 134 h, only a minor temperature drop occurred in the central region, while other areas remained stable. The reduction in regional temperature gradients led to a uniform temperature field, suggesting near-completion of the pyrolysis process. During convective heating, heat transfer was rapid, and the heat carried by the gas first diffuses to the top, then to the radial and bottom regions, causing the overall temperature to rise rapidly. This fluid-mediated heat-transfer process significantly expanded the effective pyrolysis zone and enhanced thermal utilization efficiency.

3.2. Oil and gas generation mechanisms

3.2.1. Recovery of pyrolysis oil and gas

Fig. 7 shows the variations of oil and gas production during convective heating. A total of 110 liquid samples were collected during the experiment, yielding cumulative water, oil, and gas productions of 15.20 L, 11.15 L, and 28.53 m^3, respectively. At 30 h, temperatures in most regions exceeded 136 °C, indicating the onset of water production at the outlet. At 46 h, when the temperature around the wellbore exceeded 368 °C, oil began to flow from the outlet. After 101 h, water production ceased, and only minor amounts of oil were recovered. The increase in gas production may reflect both continued primary devolatilization and

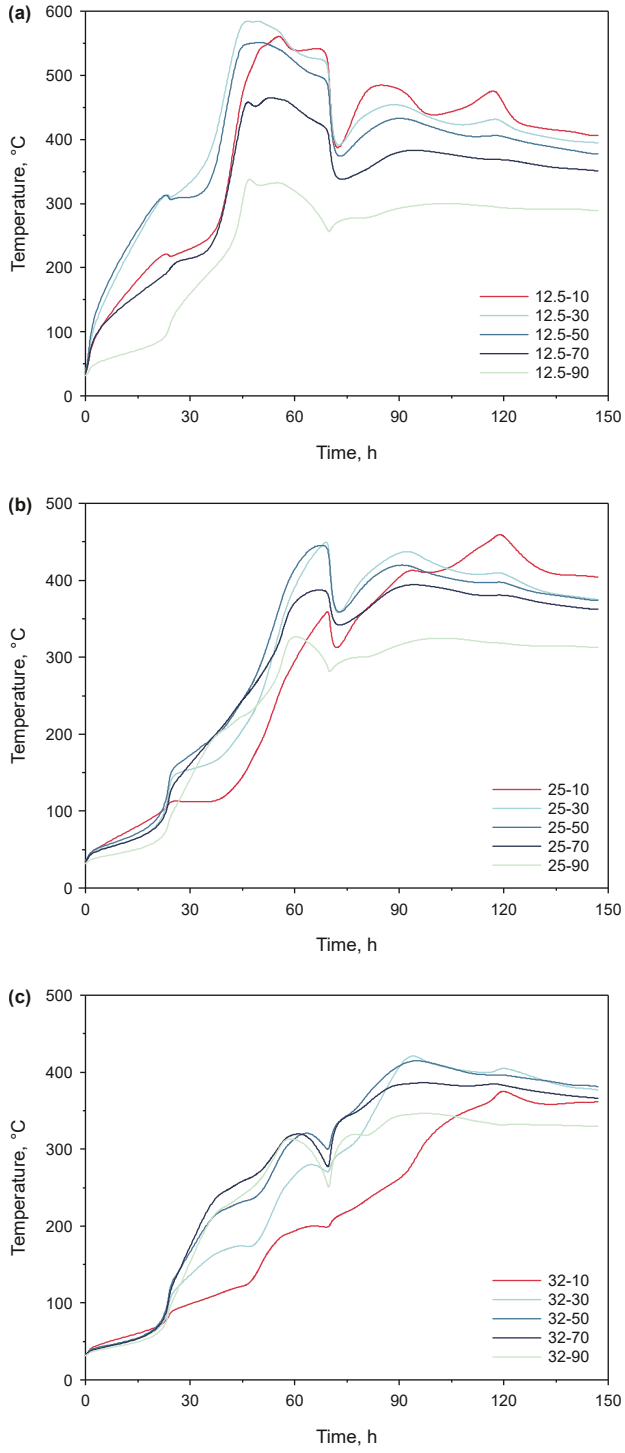


Fig. 4. Temperature variation curves during convective heating: **(a)** 12.5 cm; **(b)** 25 cm; **(c)** 32 cm.

partial secondary cracking of heavy hydrocarbons before their removal from the reactor. During convective heating, cumulative oil and gas recovery was 24.48% and 92.42%, respectively. This is mainly due to the high-temperature gas injected, which can effectively carry a large amount of pyrolysis products out of the sample, thereby reducing the products' residence time within the coal and achieving relatively complete product collection.

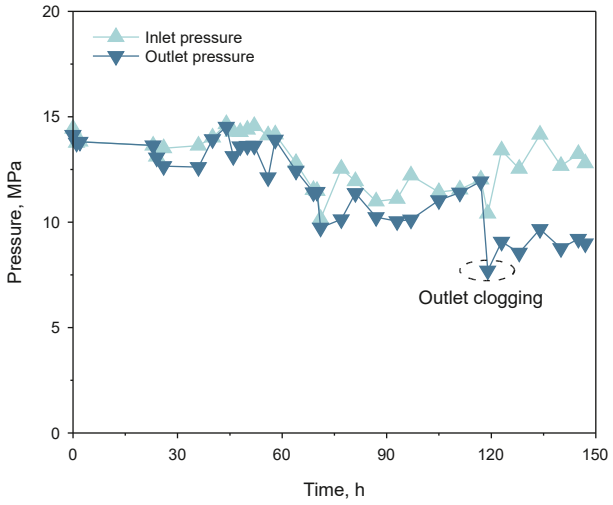


Fig. 5. The pressure variation curves during convective heating.

3.2.2. Components of pyrolysis oil

The components of the pyrolysis oil at various stages were analyzed by GC-MS, with the major components marked with distinct symbols in the figure. Fig. 8 presents the total ion chromatogram (TIC) of the pyrolysis oil collected during convective heating, showing that the primary constituents include alkanes, alkenes, aromatics, and phenols, along with other compounds such as acids, aldehydes, esters, and alcohols. For analytical convenience, the oil-production period from 46 to 147 h was divided into five stages: early, early-middle, middle, middle-late, and late. Furthermore, based on carbon number distribution and molecular weight, the oil components were classified into light oil ($C < 20$) and heavy oil ($C \geq 20$).

Fig. 8(a) presents the ion chromatograms of the pyrolysis oil during the convective heating. As the reaction progressed, the proportion of light oil ($C < 20$) increased from 76.8% in the early stage to 79.9% in the late stage, while the corresponding heavy oil ($C \geq 20$) decreased from 23.2% to 20.1%; notably, the light oil content peaked at 97.8% during the middle stage. More than 50% of the pyrolysis zone reached temperatures exceeding 426 °C. Analysis of the chromatograms indicates that the peak in light oil was primarily attributed to the cracking of heavy, long-chain components into lighter and shorter-chain hydrocarbons. conversely, from the middle to the late stage, the temperature in the near-wellbore region remained above 450 °C, resulting in a subsequent increase in heavy oil ($C \geq 20$) to 20.1%. This increase is attributed partly to aromatization and condensation reactions that formed higher-molecular-weight polycyclic aromatic compounds. The effective recovery of heavy components ($C \geq 20$) under convective heating is primarily driven by rapid thermal-fluid carryover. The continuous injection of high-velocity carrier gas significantly lowers the local partial pressure of nascent heavy volatiles, accelerating their desorption and forcefully sweeping them from the reaction zone before condensation or secondary cracking occurs (Fuentes-Cano et al., 2018). Coupled with the improved porosity and permeability in late stages, which facilitate the extraction of previously generated heavy tars, this mechanism ensures that a substantial portion of the heavy oil is recovered directly as primary pyrolysis products. Further analysis of the chemical components, as shown in Fig. 8(b), reveals that the majority of the pyrolysis zone exceeded 426 °C from the early to the middle stage, while alkane content initially increased from 6.90% to 15.09% due to the generation of short-

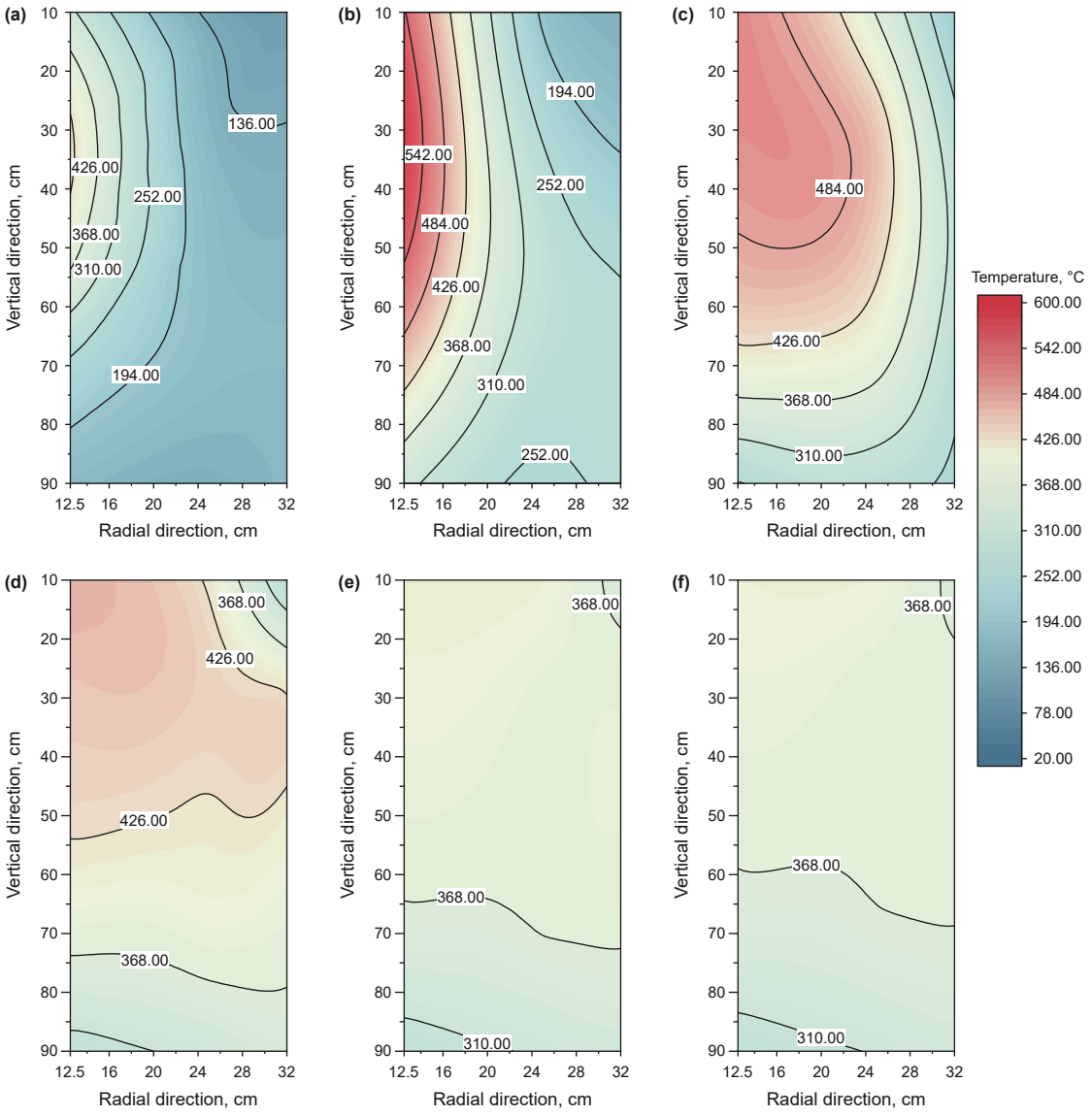


Fig. 6. The temperature field variation cloud map: **(a)** 30 h; **(b)** 46 h; **(c)** 70 h; **(d)** 93 h; **(e)** 134 h; **(f)** 147 h.

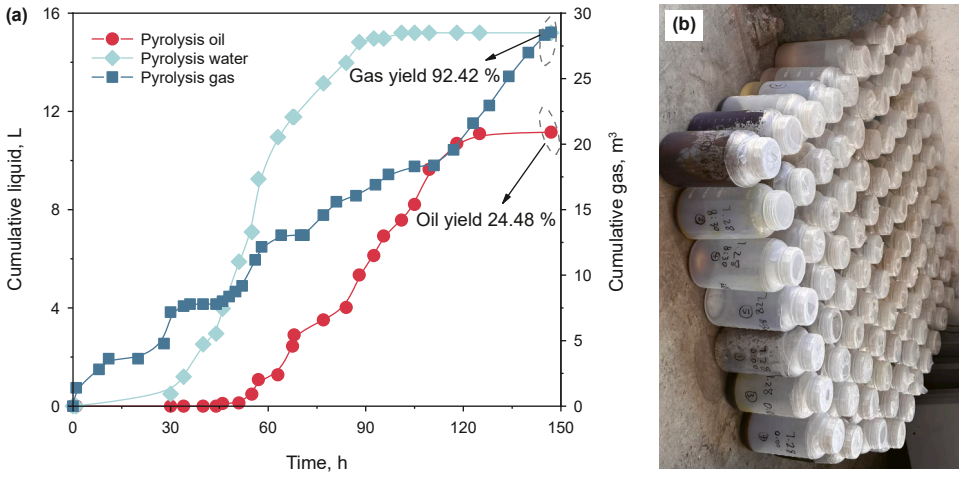


Fig. 7. Product production during convective heating: **(a)** cumulative oil, water, and gas production; **(b)** photograph of the collected pyrolysis oil.

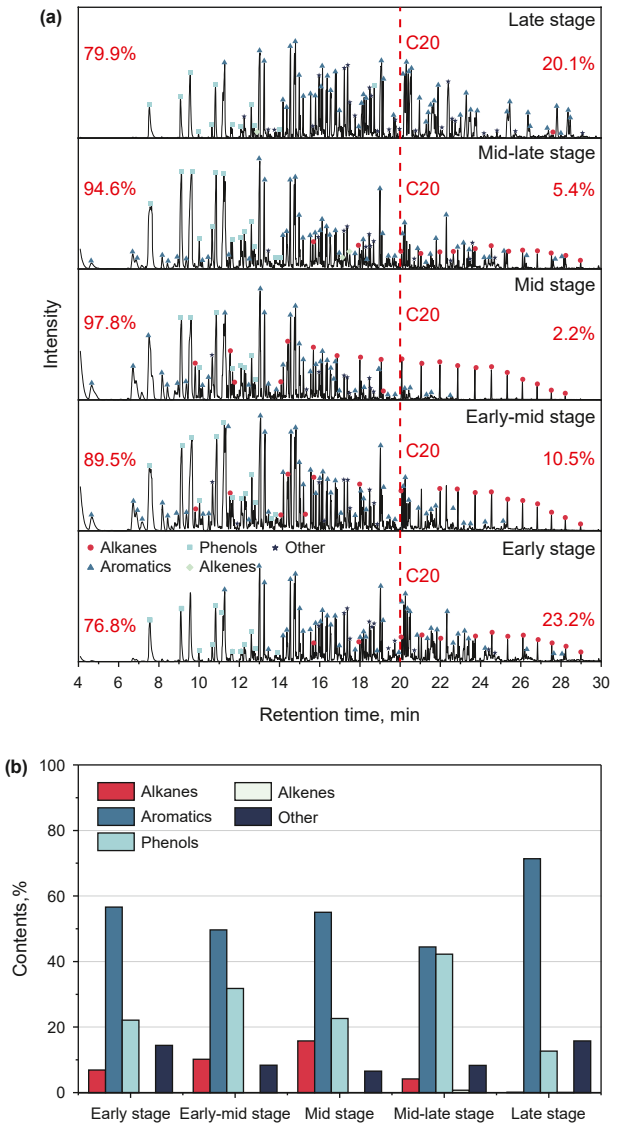


Fig. 8. Components of pyrolysis oil during convection heating. **(a)** Ion chromatogram; **(b)** Contents of each component.

chain and long-chain alkanes. The aromatic hydrocarbon content increased from an initial 56.59% to 71.39% by the late stage. While the content remained relatively stable from the early to middle stages, a decline was observed during the transition from the middle to the middle-late stage. This decrease is primarily attributed to the reaction of aromatics with oxygen-containing groups to generate phenols, and to cracking, which reduces the abundance of macromolecular hydrocarbons. However, the content rebounded in the late stage, driven by alkane aromatization, phenol dehydroxylation, and the condensation of aromatics into larger aromatic molecules. Phenols increased from 22.09% in the early stage to 42.27% in the middle-late stage, as a larger proportion of the pyrolysis zone surpassed 426 °C. This trend is attributed to the cleavage of C–O bonds in ethers and to the stabilization of oxygen-containing radicals by hydrogen radicals (Lu et al., 2024). From the middle-late stage to the late stage, the drop in phenolic compounds is mainly attributed to the dehydroxylation reaction and cracking to generate aromatics. The persistently low alkene content indicates that saturated hydrocarbons predominated over unsaturated hydrocarbons during product migration. Other compounds were present in trace amounts; their formation resulted from the decomposition of oxygenated functional groups, while their reduction was associated with CO_2 generation during pyrolysis. Under convective heating, the pyrolysis oil was dominated by light components, while heavy components were also efficiently recovered. Moreover, its composition exhibited a progressive transformation from aliphatic hydrocarbons and oxygenated compounds toward aromatic compounds.

3.2.3. Components of pyrolysis gas

Gas chromatography was employed to analyze the pyrolysis gas composition, revealing that the primary constituents include CO_2, CH_4, H_2, and H_2S, alongside minor amounts of C_2H_4 and C_2H_6; gases containing two or more carbon atoms are collectively designated as C_2–C_6. Fig. 9 shows the component of pyrolysis gas during convective heating. The CO_2 content initially decreased, then increased, and then decreased again. Before 38 h, the temperature across most of the pyrolysis zone had exceeded 136 °C. The increase in CO_2 content was mainly related to the release of physically adsorbed CO_2. As the heating progressed to 62 h, temperatures in localized regions exceeded 484 °C. The increase in CO_2 content is mainly associated with the thermal cracking of oxygenated functional groups, such as carboxyl and carbonyl groups; as pyrolysis proceeded, the CO_2 content gradually decreased after 89 h (Guo et al., 2023a). The CH_4 content initially increased rapidly, then decreased, and subsequently rose again, becoming the main gas component. From 6 to 62 h, the rise in CH_4 was linked to aliphatic side-chain cracking; however, from 62 to 97 h, while the majority of the pyrolysis zone was consistently maintained at temperatures above 426 °C, CH_4 content showed a downward trend, accompanied by an increase in C_2–C_6 content, which may be caused by the rapid cracking of long-chain hydrocarbons in tar-rich coal at high temperature.

After 97 h, the CH_4 content showed an upward trend again, and C_2–C_6 showed a downward trend again, which may be related to the secondary cracking of long-chain hydrocarbons in tar-rich coal at high temperature (Guo et al., 2023c). The H_2 content showed a trend of first rising and then declining. The initial rise between 6

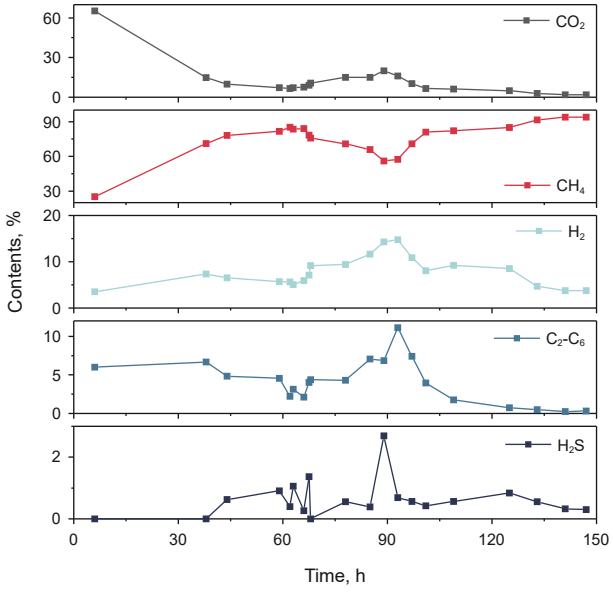


Fig. 9. Component of pyrolysis gas during the convective heating.

and 38 h is likely due to the breakage of aliphatic C–H bonds and hydrogenated aromatic structures during early pyrolysis. The rise of H_2 content after 62 h is related to the semi-coke polycondensation dehydrogenation reaction. Beyond 97 h, although the temperature in the near-wellbore region was sustained above 450 °C, the H_2 content decreased, indicating that the pyrolysis reaction tended to end as the semi-coke had transformed into a hydrogen-poor structure through polycondensation, depleting available active hydrogen sources and significantly reducing the H_2 generation rate (Kang et al., 2025). The H_2S content remained relatively stable, with a slow increase in the later stages, possibly linked to the high-temperature release of inorganic and organic sulfur. Convective heating enhanced gas mobility and accelerated pyrolysis resulting in the concentrated release of gases such as CO_2 and CH_4, relatively low H_2 content, and significant generation of secondary cracking products.

3.3. Characteristics of the reaction zones

3.3.1. Evolution characteristics of pore structure

Fig. 10 shows CT images of different zones of convective heating, and the porosity of the sample was 3.63%. The pore size of the original sample ranged from 0.68 to 84.39 μm. Based on equivalent diameter, the pore structure was categorized into three different size ranges: <1 μm, 1–10 μm, and >10 μm. In these images, pores are color-coded by size: red denotes pores with diameters >10 μm, purple indicates diameters between 1 and 10 μm, and green represents pores <1 μm. Combined with the statistical results of pore number and pore diameter distribution in different zones in Fig. 11, as the radial distance increased, both the size and number of pores decreased significantly, and the pore size distribution also narrowed. In the regions 12.5 cm and 25 cm from the wellbore, pyrolysis was strong, leading to a dense, blocky, or flaky distribution of pores >10 μm and the formation of highly interconnected seepage channels. The proportion of pores >10 μm reached 8%, and the maximum pore diameter was 245 μm. In the outer regions of 32 cm (such as 32-10, 32-30, 32-90), it only showed a small number of isolated, slender cracks, pore size distribution narrowed significantly, the proportion of pores >10 μm was less than 2%, the maximum pore diameter was 75 μm, mainly <10 μm pores, corresponding to significantly reduced pyrolysis intensity. In the vertical direction, the region from 30 to 70 cm is the main pyrolysis zone. Pyrolysis was most complete within the 30–50 cm range, where local coalescence of 1–10 μm pores into those >10 μm was observed. In contrast, pore-scale features in the 10 cm and 90 cm end areas decreased significantly, with mostly scattered cracks and isolated small pores, and the pore-size distribution was mostly <1 μm, mainly due to spatially nonuniform pyrolysis (Xu et al., 2021). In summary, gas flow during convective heating accelerated heat transfer, creating a radially concentrated, vertically oriented high-temperature pyrolysis reaction zone near the center and within the middle section (Geng et al., 2017). The significantly enhanced connectivity makes this zone the primary pathway for oil and gas migration and production. In contrast, significant heat attenuation occurred in the outer and bottom regions, where the pore structure remained dominated by pores <1 μm. Additionally, fluid migration played a key physical role in pore expansion by enhancing the uniformity of heat transfer, facilitating the removal of pyrolysis products, and maintaining relatively high pore pressure, thereby reducing effective stress and promoting pore expansion, connectivity enhancement, and local pore development during convective heating (Guo et al., 2026; Li et al., 2024).

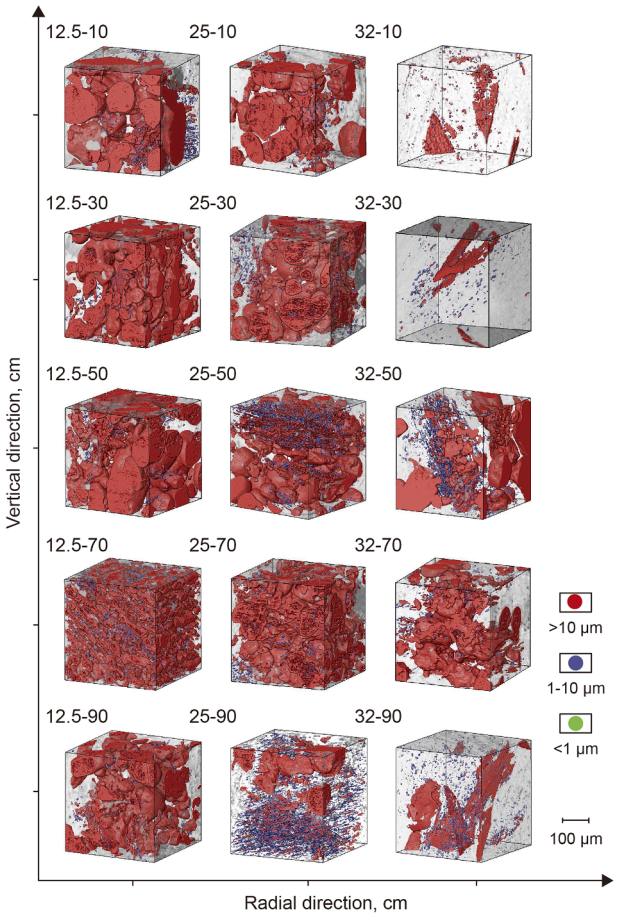


Fig. 10. CT images of different zones after convective heating.

The permeability throughout the convective heating process is calculated using Eq. (1), which is derived from Darcy's law for compressible fluids:

$$K = \frac{Q_0 P_0 \mu \ln\left(\frac{d_e}{d_w}\right)}{\pi h\left(P_1^2 - P_2^2\right)} \tag{1}$$

where Q_0 is the gas flow rate, m^3/s; P_0 is the reactor pressure, Pa; μ is the gas viscosity, Pa·s; d_e and d_w are the outer and inner diameters, respectively, m; h is the medium thickness, m; P_1 and P_2 represent the inlet and outlet pressures, respectively, Pa; and K is the permeability, m^2.

Fig. 12 shows the variation curve of permeability during convective heating. At 36 h, as temperatures across most regions exceeded 136 °C, the permeability reached 30.84 mD. This initial thermal elevation promoted the decomposition of organic matter, the release of moisture, and the early formation of volatiles, thereby inducing the formation of initial micropores and localized thermal fractures. At 46 h, as the average temperature in the near-wellbore region exceeded 454 °C, the coal entered a pronounced pyrolysis stage. This phase was marked by the onset of oil production and a continuous increase in permeability. By 101 h, with temperatures throughout the pyrolysis zone exceeding 426 °C, the permeability peaked at 81.43 mD. According to the effective stress principle, the elevated pore pressure significantly reduced the effective stress acting on the coal matrix, thereby mechanically promoting the dilation of pores and fractures. This permeability

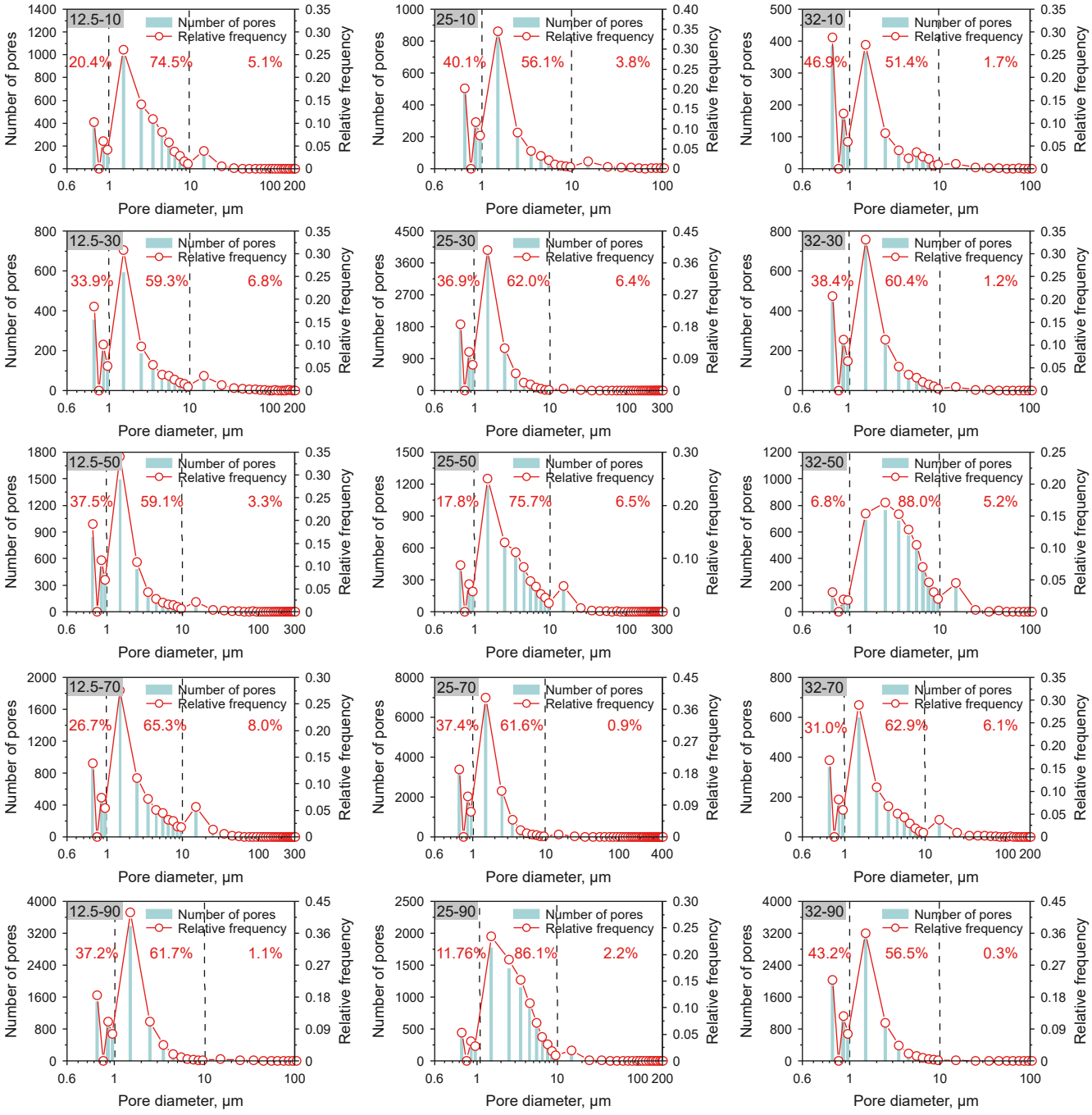


Fig. 11. Pore number and pore diameter distribution at different zones after convective heating.

peak closely coincided with the stage of intensive oil and gas expulsion, indicating that both organic-matter pyrolysis and structural expansion had reached their maximum extent. Subsequently, the permeability began to decline. This reduction is primarily attributed to the migration, retention, and localized redeposition of heavy components within the newly evolved pore network (Xu et al., 2023b). By 147 h, although the overall reactor temperature was sustained above 368 °C, the permeability had decreased to 12.70 mD. The average permeability was 42.90 mD during convective heating. The injected fluid improved heat-transfer uniformity and promoted the timely removal of pyrolysis products. Furthermore, the fluid flow in the pores sustained elevated pore pressure and consequently preserved high flow conductivity.

Fig. 13 presents cloud maps of porosity and permeability after convective heating. High-porosity regions are mainly concentrated in the near-well high-temperature zone, where the maximum porosity reaches 30.1% in the 12.5–30 cm interval. Overall, porosity in the central region generally exceeds 14%, accounting for approximately 60% of the total volume. In contrast, pore development in the distal edge regions (e.g., 32-10 and 32-90) is much weaker, with a minimum value of only 0.54%. These results indicate that the temperature field is the primary controlling factor for pore expansion. More intense

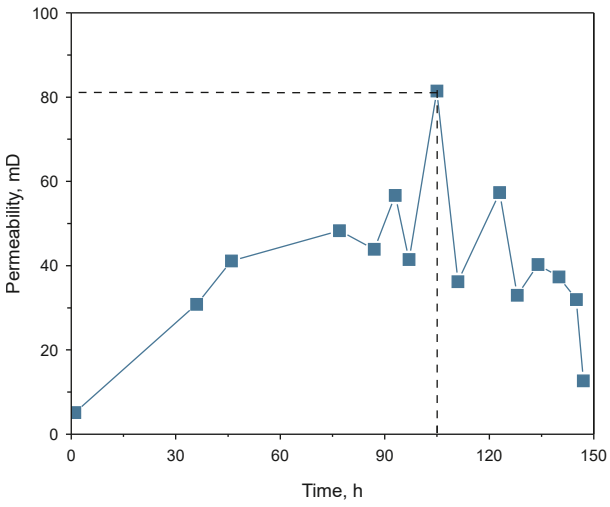


Fig. 12. Permeability variation during convective heating.

pyrolysis and volatile release in the near-well high-temperature zone significantly promote pore development, whereas pore growth is clearly limited in the low-temperature peripheral region. Combined with permeability cloud maps and quantitative analysis, the results further show that pore development is reflected not only in increased porosity but also in the formation of effective seepage channels. Driven by the injection–production pressure differential, the directional sweeping effect of the convective fluid enhances pore-network connectivity. It induces the development of high-permeability structures with a degree of directional anisotropy. As a result, the high-porosity central zone shows good spatial consistency with the high-permeability core zone, where local permeability exceeds 400 mD. This coupled evolution of pore expansion, connectivity enhancement, and directional seepage structure significantly reduces flow resistance and transport tortuosity, thereby facilitating the rapid removal of primary oil and gas products from the high-temperature reaction zone (Zhu et al., 2026). Consequently, the retention, condensation, and further secondary reactions of heavy components are suppressed to some extent, which is favorable for improving the overall oil and gas recovery efficiency.

3.3.2. Evolution characteristics of organic matter

Fig. 14 shows the distribution cloud map of organic matter after convective heating. High S1 values were concentrated mainly in the upper region, with a maximum of 42.23 mg/g. This indicates that the oil and gas products generated by pyrolysis exhibit a pronounced tendency for upward migration. During pyrolysis, the generated oil vapors and gases migrated through the evolving pore network, similar to conductive heating. However, the carrying and displacement effects of the convective fluid make this migration and accumulation effect more pronounced. Relatively high S2 values were observed mainly in the upper and lower regions. The maximum value of S2 at the top can reach 95.06 mg/g. This phenomenon is related to the incomplete conversion of organic matter at low temperatures. Additionally, the maximum S2 value at the bottom reached 44.18 mg/g. This accumulation is partly attributable to the local temperature remaining below 368 °C; more critically, it may also be related to the enrichment and retention of heavy components that are difficult to crack as they move downward with the fluid. Convective heating facilitates efficient pyrolysis of organic matter with minimal blockage. However,

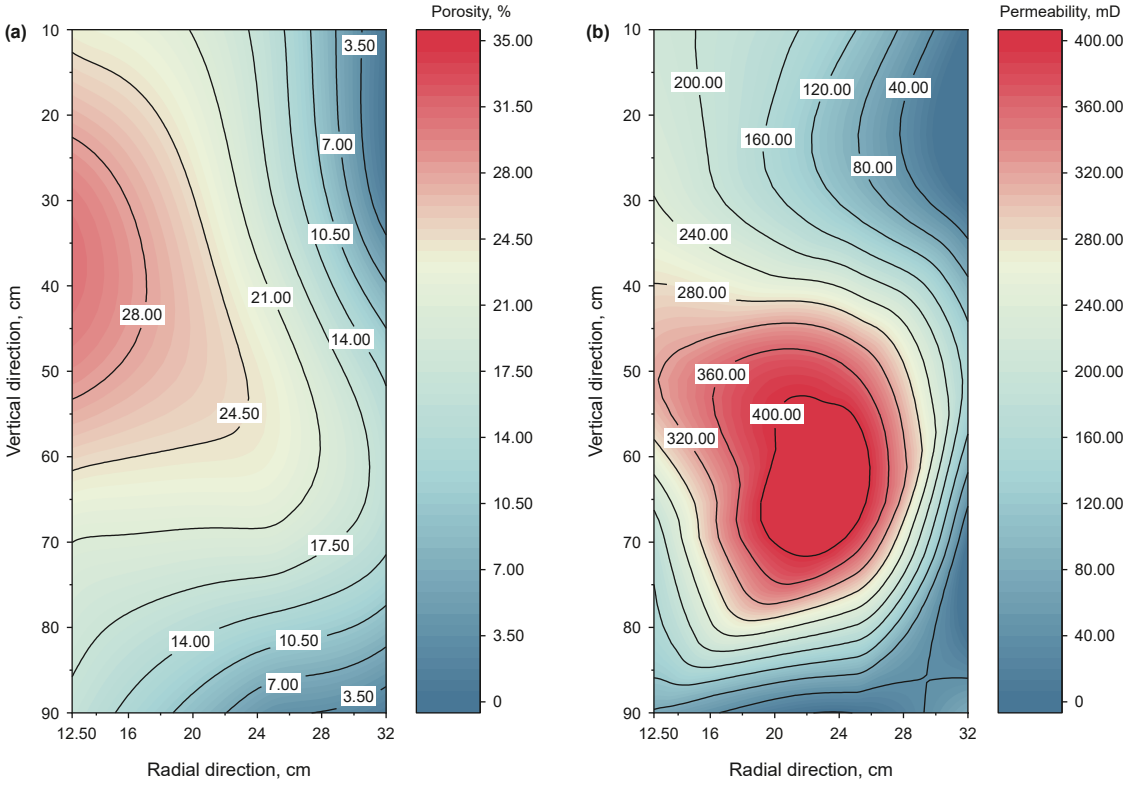


Fig. 13. Cloud maps of porosity and permeability after convective heating.

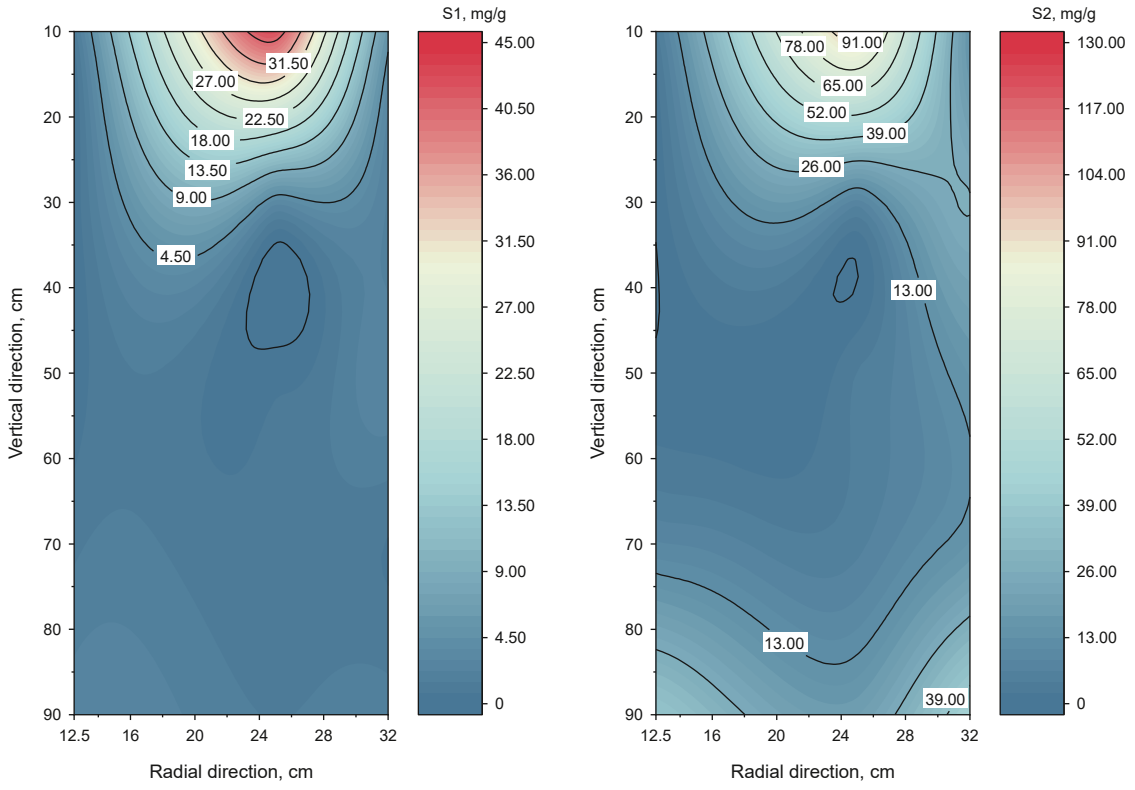


Fig. 14. Organic matter distribution cloud map after convective heating.

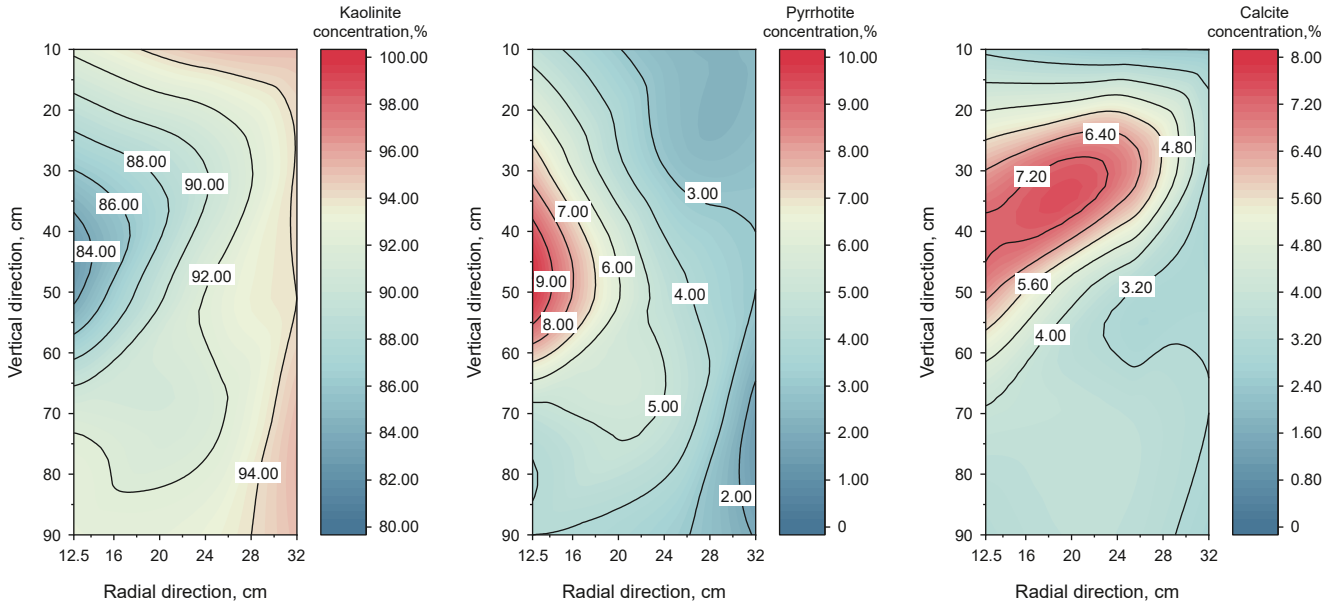


Fig. 15. Inorganic minerals distribution cloud map after convective heating.

incomplete cracking may still occur in localized low-temperature regions.

3.3.3. *Evolution characteristics of inorganic minerals*

Fig. 15 shows the distribution cloud map of inorganic minerals after convective heating. Neither pyrite nor tobelite was detected in the sample, suggesting that these minerals were extensively transformed under the present experimental conditions. Within the 300–600 °C range, tobelite transforms into an amorphous aluminosilicate via deammoniation and dehydroxylation reactions (Eq. (2)); convective heating significantly accelerated this decomposition, resulting in the complete conversion of tobelite (Zhang et al., 2016). Kaolinite undergoes dehydroxylation between 450 and 600 °C to form metakaolinite (Eq. (3)) (Liu et al., 2015),

resulting in the destruction of its crystal structure and the disappearance of its characteristic diffraction peaks. The pyrolysis in the area around the wellbore is sufficient, where the relative content of kaolinite was significantly lower than in distal areas, consistent with the high-temperature thermal evolution characteristics of this zone. Pyrite thermally decomposed completely into pyrrhotite (Eq. (4)) (Boyabat et al., 2004). Pyrrhotite ($Fe_{11}S_{12}$) is thermally stable up to approximately 600–700 °C. Its content peaked at 9.94% in the 12.5–50 cm region. Calcite has high thermal stability, and no decomposition products were detected. Its content change is mainly affected by relative enrichment. In summary, the high-temperature fluid in convective heating promoted the decomposition of tobelite, kaolinite, and pyrite, leading specifically to the extensive transformation of tobelite.

$$NH_4Al_2(Si_3Al)O_{10}(OH)_2 \rightarrow Al_2O_3 \cdot xSiO_2 + NH_3 + H_2O \quad (2)$$

$$Al_2Si_2O_5(OH)_4 \rightarrow Al_2Si_2O_7 + 2H_2O \quad (3)$$

$$FeS_2 \rightarrow Fe_{11}S_{12} + S\uparrow \quad (4)$$

3.4. Discussion

3.4.1. Migration mechanisms during in-situ convective pyrolysis of tar-rich coal

Fig. 16 shows the tar-rich coal in-situ pyrolysis migration mechanism during convective heating, compared to conductive heating. Convective heating utilizes high-temperature fluids as heat carriers, while the advancement of the pyrolysis front shares similarities; however, convective effects significantly alter pore evolution and product migration patterns. The process can be divided into three stages: (a) thermal expansion and release of the light component. When the temperature is below 300 °C, thermal expansion of the coal matrix triggers thermal fracturing, initiating the gradual release of volatiles. In the near-wellbore region where temperatures exceed 400 °C, organic matter undergoes pyrolysis, generating hydrocarbon gases and light oil that migrate, converge, and are ultimately produced. Additionally, fluid flow within the pores provides structural support, inhibiting pore throat closure after pyrolysis and thereby maintaining high permeability. (b) rapid pyrolysis stage. As the near-wellbore temperature rises above 450 °C, kerogen pyrolysis intensified, substantially increasing the generation of oil vapors and hydrocarbon gases and further expanding the pore-throat structure. Concurrently, temperatures in most of the central heating zone exceed 400 °C, promoting deep pyrolysis of kerogen. The well-connected pore network ensures the effective migration and output of pyrolysis products toward the bottom production well. (c) stable pyrolysis stage. With temperatures in most regions exceeding 400 °C, kerogen undergoes deep pyrolysis and structural reorganization. This stage involves polycondensation reactions that form macromolecular coke, alongside the secondary cracking of heavy pyrolysis products into smaller molecules. Some macromolecular products condense in the low-temperature zone, leading to local pore blockage and reduced reservoir

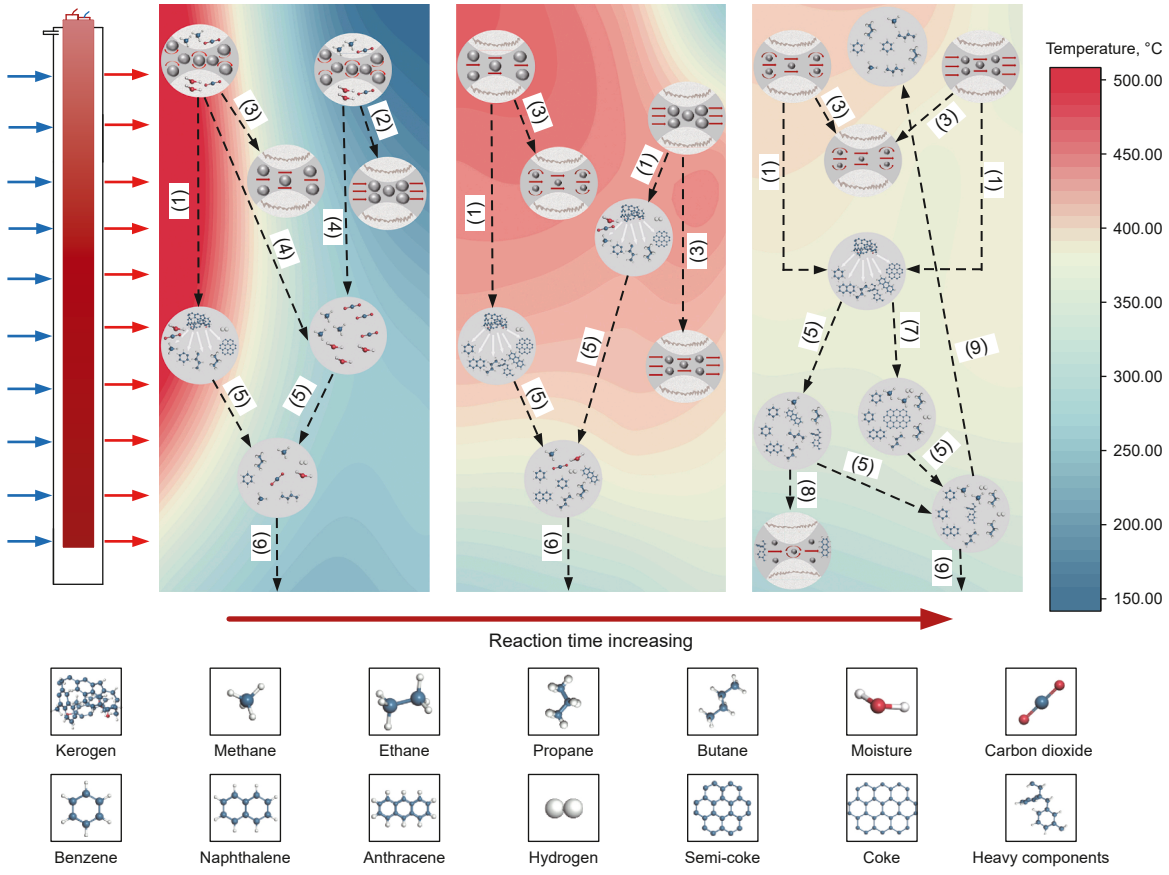


Fig. 16. Schematic of product-generation and migration mechanisms during in-situ convective pyrolysis.

permeability. Owing to fluid convection, entrainment, and displacement, the overall permeability remains higher. Additionally, certain pyrolysis products migrated upward because of their lower density, leading to accumulation at the top. By injecting high-temperature fluids, convective heating enables rapid heat transfer, effectively overcoming the limitations of conductive heating and preventing overly concentrated heat near the wellbore, thereby significantly enhancing overall pyrolysis efficiency. The fluid-carrying effect not only promoted the release of oil and gas products but also alleviated pore blockage caused by macromolecular polycondensation. However, in the low-temperature bottom area, some macromolecular compounds may remain, which need to be considered in the optimization of future exploitation regimes.

3.4.2. Comparison between convective and conductive heating for in-situ pyrolysis of tar-rich coal

The core of in-situ pyrolysis of tar-rich coal depends on efficient heat injection and smooth product output. Although convective and conductive heating share similarities in advancing the pyrolysis front, they differ in heat transfer mechanisms, the evolution of temperature and pressure fields, product characteristics, and reservoir properties (Wang et al., 2024). Conductive heating relies primarily on thermal conduction within the coal matrix; however, the low thermal conductivity of tar-rich coal limits heat transfer rates, resulting in prolonged heating cycles. As shown in Fig. 17(a), conductive heating required 482 h to complete pyrolysis, with an average heating rate of only 0.70 °C/h. It also generated steep temperature gradients, leading to overheating in the near-wellbore region and pronounced thermal lag in the distal areas. In contrast, convective heating uses a high-temperature fluid as a heat carrier, substantially enlarging the heat-transfer interface through fluid–solid exchange and promoting deeper heat penetration. As a result, the average heating rate increased from 0.70 to 2.24 °C/h, corresponding to a 3.2-fold increase, while the pyrolysis duration decreased from 482 to 147 h (a reduction of approximately 69.5%). To further quantify these spatial and thermal advantages, the effective pyrolysis volume fraction (V_{eff}) and the temperature-gradient decay rate were introduced. Here, V_{eff} is defined as the ratio of the volume with temperatures above 429 °C to the total effective reactor volume. A temperature of 429 °C was experimentally identified as the threshold for intense pyrolysis. Under conductive heating, V_{eff} reached only 7.7% at the stage of strongest pyrolysis (342 h). By contrast, the high-temperature convective fluid significantly expanded the affected region, increasing V_{eff} to 23.6%, corresponding to a 3.06-fold enlargement of the intense pyrolysis zone. More importantly, convective heating accelerated the homogenization of the temperature field (Shui et al., 2024). Under conductive heating, the temperature gradient decreased from a peak of 1021.0 °C/m at an average rate of 3.9 °C/(m·h), and 221 h was required to reach the specified homogenization criterion. Under convective heating, however, the decay rate increased to 20.1 °C/(m·h), which was 5.15 times the value under conductive heating. Within only 101 h, the relative homogenization amplitude reached 95.7%, indicating that the steep thermal gradients were effectively mitigated in less than half the time required under conductive heating. These quantitative results demonstrate that the superiority of convective heating is not merely reflected in faster heating and earlier hydrocarbon production, but more fundamentally in its ability to substantially enlarge the effective pyrolysis zone and accelerate temperature-field homogenization. In addition, as shown in Fig. 17(b), fluid injection significantly altered the pressure field. The strong displacement effect of convective heating, synchronized with oil, gas, and water production, was observed as a function of heating rate, as shown in Fig. 17(c); rapid production was achieved within 147 h. In contrast, conductive heating did not initiate oil generation until 249 h, representing a delay of 203 h compared to the convective heating. The cumulative oil and gas yields from convective heating were 12.42 and 3.27 times those from conductive heating, respectively. Under convective heating, the dominant flow direction of the thermal fluid dictates the high spatial

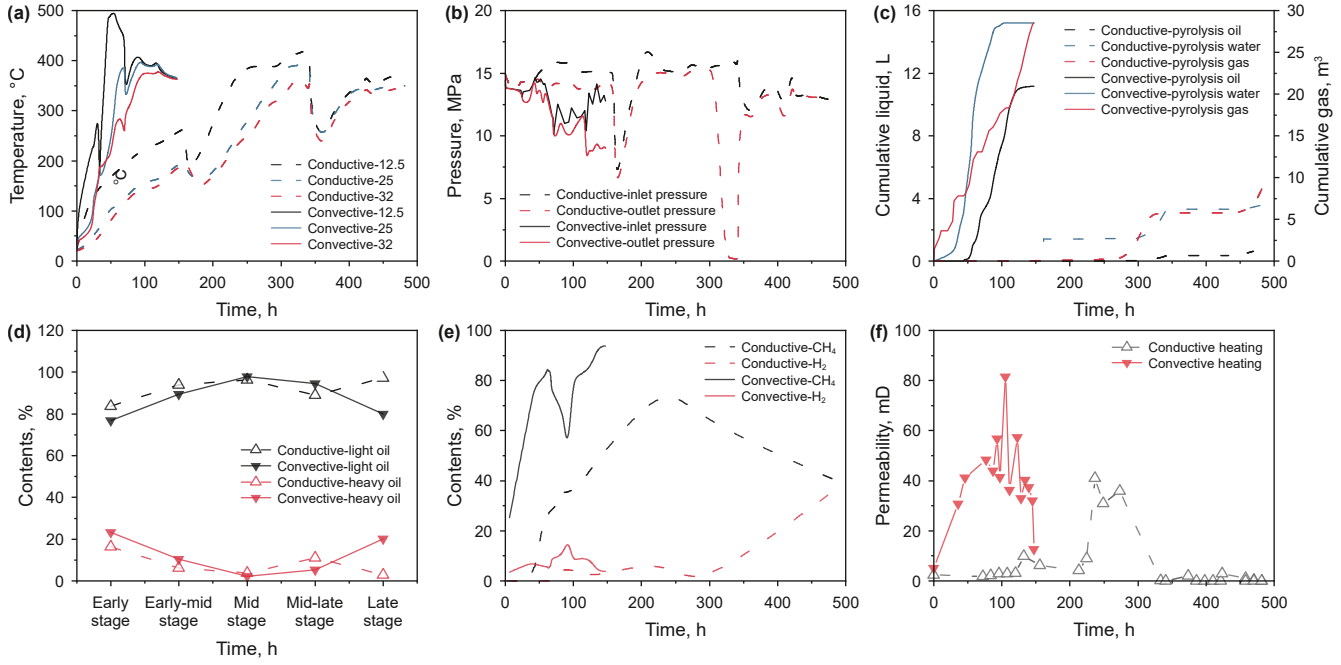


Fig. 17. Comparison between conductive and convective heating: **(a)** temperature; **(b)** pressure; **(c)** oil and gas production; **(d)** pyrolysis oil component; **(e)** pyrolysis gas component; **(f)** permeability.

overlap among the preferential heating, pyrolysis, and pore-enhancement zones. This flow-oriented guidance not only governs the spatial distribution of pyrolytic reactions but also drives the early production of hydrocarbons through efficient carrying effects, thereby significantly shortening the overall recovery cycle.

As shown in Fig. 17(d) and (e), the product compositions from convective and conductive heating exhibit stark differences, fundamentally stemming from the distinct residence times of primary pyrolysis products in the high-temperature zone. Compared to conductive heating, convective heating exerts a powerful inhibitory effect on secondary cracking and retention reactions by significantly shortening this residence time. Under conductive heating, the lack of fluid carryover results in the slow expulsion of heavy tar. This prolonged high-temperature exposure forces primary macromolecules to undergo severe secondary cracking (yielding light hydrocarbons and gases) and retention reactions (such as aromatization, polycondensation, and coking). This is evidenced by the higher content of light components in the conductive-heating oil and the significant increase in H_2 content during its later stages. Conversely, the rapid sweeping effect of convective heating enables the instantaneous extraction of heavy products upon their generation (Zhu et al., 2026). By fundamentally blocking secondary thermal cracking pathways and effectively preventing product retention and condensation within the pore network, convective heating yields a higher heavy oil content. Correspondingly, its gas production is dominated by CH_4 with negligible H_2 content, firmly confirming that the thermal fluid facilitates the timely extraction of macromolecular products while suppressing severe late-stage polycondensation. As shown in Fig. 17(f), convective heating maintained an average permeability of 42.90 mD, which was 7.96 times the value measured under conductive heating (5.39 mD). Furthermore, the local maximum porosity reached 30.1% after convective heating, compared to 9.36% for conductive heating. Convective heating established high-conductivity channels conducive to subsequent exploitation. Analysis of the upper regions reveals elevated S1 values for both heating methods, indicating the upward migration and accumulation of low-density hydrocarbons. Notably, convective heating achieved a significantly stronger top-enrichment effect. Its peak S1 value reached 42.23 mg/g, 2.08 times that of conductive heating (20.35 mg/g), demonstrating a clear advantage in facilitating the upward migration of light hydrocarbons. Conversely, conductive heating resulted in severe heavy residue accumulation at the reactor base, evidenced by a peak S2 of 119.68 mg/g. This value is 2.71 times higher than the 44.18 mg/g observed under convective heating, a stagnation that fundamentally restricts the continuous expulsion of oil and gas. Furthermore, convective heating significantly accelerated the thermal decomposition and phase transformation of inorganic minerals, as highlighted by the complete conversion of tobelite. Under convective conditions, the peak pyrrhotite content reached 9.94%, 4.46 times greater than that under conductive heating (2.23%), while kaolinite contents remained comparable (95.24% vs. 94.57%). The high-temperature fluid effectively drives these mineral-phase transformations, creating optimal conditions for pore-network evolution and subsequent fluid flow. Ultimately, by synergistically enhancing both heat and mass transfer, convective heating delivers markedly superior pyrolysis efficiency and product recovery. This approach ensures uniform heat injection while facilitating unimpeded product extraction, thereby significantly enhancing the overall efficiency of in-situ pyrolysis of tar-rich coal.

3.4.3. Engineering practice guidelines

Based on the evolution of the temperature field, product migration behavior, and pore-structure development observed in large-scale three-dimensional physical simulation experiments, some preliminary engineering implications can be drawn for the in-situ pyrolysis of tar-rich coal under convective heating. In terms of well-layout design, the experimental results indicate that both the high-temperature fluid and volatile pyrolysis products exhibit a clear upward migration tendency during convective heating, resulting in a more pronounced enrichment of low-density hydrocarbons in the upper part of the coal seam. Therefore, a multistage fractured horizontal well configuration may be preferentially considered for field application. In this configuration, the injection/heating well is preferably located in the middle-to-lower part of the coal seam to enhance vertical heat and mass transfer efficiency. In contrast, production wells may be located at both the top and bottom of the coal seam. The upper production well facilitates the recovery of light hydrocarbons enriched in the upper zone. In contrast, the bottom production well helps discharge accumulated fluids from the lower zone, reducing the risk of heavy-residue retention and local blockage. In terms of key engineering parameters, the experimental results show that when the temperature in most regions of the coal body exceeds 426 °C, organic matter pyrolysis is significantly accelerated and the post-pyrolysis pore structure becomes better developed, which is favorable for oil and gas generation and migration. Therefore, considering both pyrolysis effectiveness and engineering feasibility, a field operating temperature range of 426–500 °C is recommended as a preliminary reference.

It should be noted that the above engineering implications should be interpreted with caution, because scale effects between the experimental system and actual subsurface operations are unavoidable. Although the present system reproduces the essential features of in-situ pyrolysis, including unsteady convective heat transfer, fluid-driven product migration, and reservoir-level pressure conditions, significant differences remain between the sub-meter experimental model and field-scale reservoirs. These differences are mainly reflected in three aspects. First, fluid migration distances in the field may extend from tens to hundreds of meters. Such long-distance migration may enhance the secondary cracking of heavy tar during prolonged high-temperature residence, thereby reducing heavy-oil yield while increasing the proportion of lighter oil and gas (Wang et al., 2022). It may also increase the risk of downstream condensation, local blockages, and a decline in dynamic permeability. Second, unlike the nearly adiabatic boundary of the physical model, actual reservoirs are bounded by roof and floor strata that act as large, continuous heat sinks, leading to greater boundary heat loss. Third, whereas the experimental medium is relatively homogeneous and favors a more uniform thermal sweep, field reservoirs are inherently more heterogeneous, which can strongly control fluid flow and induce fingering, preferential channeling, premature thermal breakthrough, and unheated dead zones. Therefore, the present results are more suitable for revealing the relative mechanistic advantages of convective heating over conductive heating, particularly in terms of enhanced heat transfer, enlargement of the effective pyrolysis zone, and improved product migration conditions, rather than serving directly as field-design criteria. Although this study demonstrates the clear mechanistic advantages of convective heating, key engineering parameters, such as well spacing, injection–production pressure differential,

and fluid flow rate, still need to be optimized on a case-by-case basis, in combination with reservoir heterogeneity and numerical simulation.

4. Conclusion

This study used a self-developed high-temperature and high-pressure experimental apparatus to conduct in situ pyrolysis experiments on tar-rich coal under convective heating, systematically investigating the temperature and pressure evolution, oil and gas generation mechanisms, and characteristics of the reaction zones, followed by a comparative analysis with conductive heating. The main conclusions are as follows.

(1) Convective heating significantly enhanced both pyrolysis efficiency and spatial sweep. The average heating rate reached 2.24 °C/h, which was 3.2 times that under conductive heating; meanwhile, the temperature-field homogenization rate was 5.15 times that under conductive heating, and the effective intense-pyrolysis volume fraction increased from 7.7% to 23.6%. Fluid flow facilitated rapid radial heat transfer and deeper penetration, resulting in an effective pyrolysis zone that was significantly superior to that of conductive heating. Internal pressure fluctuations were significant, with an average pressure differential of 1.31 MPa.

(2) Convective heating significantly enhanced oil and gas recovery, driven by the strong dynamic carryover effect. The onset of oil production occurred 203 h earlier than in the conductive heating case. Cumulative oil and gas yields reached 24.48% and 92.42%, which were 12.42 times and 3.27 times the corresponding values under conductive heating, respectively. The pyrolysis oil contained a higher content of heavy components ($C \geq 20$), while CH_4 dominated the gas component with negligible H_2.

(3) The supporting effect of the fluid effectively maintained reservoir conductivity. The average permeability during the heating process was maintained at 42.90 mD, which was 7.96 times the value under conductive heating; the local maximum porosity after pyrolysis reached 30.1%, and the area with porosity exceeding 14% accounted for 60%, forming good seepage channels conducive to oil and gas migration.

(4) High-temperature fluids significantly promoted inorganic mineral decomposition and product migration. Convective heating accelerated the decomposition of tobelite, kaolinite, and pyrite, with tobelite being extensively transformed. Low-density hydrocarbon products exhibited a pronounced upward migration tendency, with free hydrocarbon (S1) enrichment at the top reaching 42.23 mg/g. The maximum measured S2 value in the lower region was 44.18 mg/g, suggesting that convective heating helped reduce the retention of heavy products in low-temperature regions. These results preliminarily suggest that a well configuration involving injection in the middle-to-lower section and production from both the upper and lower sections may improve recovery efficiency.

CRediT authorship contribution statement

Yan-Wei Li: Writing – review & editing, Writing – original draft, Methodology, Investigation, Formal analysis, Data curation. **Chao-Fan Zhu:** Writing – review & editing, Software, Resources. **Yi-Jian Zeng:** Resources, Methodology, **Han Tian:** Software, Methodology, Investigation. **Tian-Le Zhang:** Methodology, Investigation, Formal analysis. **Wei Guo:** Writing – review & editing, Funding acquisition.

Data availability

Data will be made available on request.

Conflict of interest

The authors declare that they have no known competing financial interests or personal relationships that could have appeared to influence the work reported in this paper.

Acknowledgment

We acknowledge financial support offered by the Key R&D project of Jilin Provincial Science and Technology Department (Grant No. 20230203121SF) and the National Oil Shale Exploitation R&D Center Open Fund Project (Grant No. 33550000-24-ZC0613-0055).

References

Boyabat, N., Özer, A.K., Bayrakçeken, S., Gülaboğlu, M.Ş., 2004. Thermal decomposition of pyrite in the nitrogen atmosphere. Fuel Process. Technol. 85 (2), 179–188. https://doi.org/10.1016/S0378-3820(03)00196-6.

Chang, Z., Wang, C., Kuang, W., Tang, Y., Wu, X., Liu, S., 2024. Product characterization and pore structure evolution of a tar-rich coal following pyrolysis under nitrogen, steam/nitrogen, and oxygen/nitrogen atmospheres. J. Anal. Appl. Pyrolysis 180, 106563. https://doi.org/10.1016/j.jaap.2024.106563.

Chen, M., Wang, C., Yuan, T., Ning, X., Huang, X., Deng, L., Che, D., 2025. Experimental investigation on gas-liquid–solid tri-phase product distributions during the simulated in-situ pyrolysis of tar-rich coal. Fuel 381, 133465. https://doi.org/10.1016/j.fuel.2024.133465.

Deng, S., Wang, Z., Gu, Q., Meng, F., Li, J., Wang, H., 2011. Extracting hydrocarbons from Huadian oil shale by sub-critical water. Fuel Process. Technol. 92 (5), 1062–1067. https://doi.org/10.1016/j.fuproc.2011.01.001.

Fuentes-Cano, D., Salinero, J., Haro, P., Nilsson, S., Gómez-Barea, A., 2018. The influence of volatiles to carrier gas ratio on gas and tar yields during fluidized bed pyrolysis tests. Fuel 226, 81–86. https://doi.org/10.1016/j.fuel.2018.03.171.

Gao, S., Zhao, J., Wang, Z., Wang, J., Fang, Y., Huang, J., 2013. Effect of CO_2 on pyrolysis behaviors of lignite. J. Fuel Chem. Technol. 41 (3), 257–264. https://doi.org/10.1016/S1872-5813(13)60017-1.

Geng, Y., Liang, W., Liu, J., Cao, M., Kang, Z., 2017. Evolution of pore and fracture structure of oil shale under high temperature and high pressure. Energy Fuels 31 (10), 10404–10413. https://doi.org/10.1021/acs.energyfuels.7b01071.

Guo, W., Li, Y., Lei, J., Tian, H., Deng, S., Li, Q., Zhu, C., 2026. Influence of fracture parameters on the development performance of in situ oil shale conversion. Energy Fuels 40 (7), 3562–3579. https://doi.org/10.1021/acs.energyfuels.5c05683.

Guo, W., Pan, J., Zhang, X., Deng, S., Zhu, C., 2023a. Experimental and mechanistic study on isothermal oxidative pyrolysis of oil shale. J. Anal. Appl. Pyrolysis 175, 106215. https://doi.org/10.1016/j.jaap.2023.106215.

Guo, W., Sun, Y., Li, Q., Zhu, C., Deng, S., Wang, Y., Liu, Z., Chen, C., Liu, B., 2023b. Experimental study and pilot tests of autothermic pyrolysis in situ conversion process for oil shale recovery. In: SPE Annual Technical Conference and Exhibition. SPE-214808-MS. https://doi.org/10.2118/214808-MS.

Guo, W., Yang, Q.C., Deng, S.H., Li, Q., Sun, Y.H., Su, J.Z., Zhu, C.F., 2022. Experimental study of the autothermic pyrolysis in-situ conversion process (ATS) for oil shale recovery. Energy 258, 124878. https://doi.org/10.1016/j.energy.2022.124878.

Guo, W., Zhang, X., Sun, Y., Li, Q., Liu, Z., 2023c. Migration mechanism of pyrolysis oil during oil shale in situ pyrolysis exploitation. Energy 285, 128769. https://doi.org/10.1016/j.energy.2023.128769.

Hefta, R., Schobert, H., 1986. Calorimetric pyrolysis of a North Dakota lignite. Fuel 65 (9), 1196–1202. https://doi.org/10.1016/0016-2361(86)90229-2.

Ju, Y., Zhu, Y., Zhou, H., Ge, S., Xie, H., 2021. Microwave pyrolysis and its applications to the in situ recovery and conversion of oil from tar-rich coal: an overview on fundamentals, methods, and challenges. Energy Rep. 7, 523–536. https://doi.org/10.1016/j.egyr.2021.01.021.

Kang, Z., Huang, D., Zhao, J., Fan, S., Yang, D., Lu, Y., 2025. Hydrogen transfer and reaction mechanism during in-situ pyrolysis of fushun oil shale with steam injection. Fuel 381, 133583. https://doi.org/10.1016/j.fuel.2024.133583.

Kang, Z., Zhao, Y., Yang, D., 2020a. Review of oil shale in-situ conversion technology. Appl. Energy 269, 115121. https://doi.org/10.1016/j.apenergy.2020.115121.

Kang, Z., Zhao, Y., Yang, D., Tian, L., Li, X., 2020b. A pilot investigation of pyrolysis from oil and gas extraction from oil shale by in-situ superheated steam injection. J. Pet. Sci. Eng. 186, 106785. https://doi.org/10.1016/j.petrol.2019.106785.

Li, M., Cheng, X., Hao, J., Lu, Z., Wei, J., 2024. Experimental and numerical investigation on the heat and mass transfer performance of tar rich coal in-situ pyrolysis. Int. J. Heat Fluid Flow 107, 109412. https://doi.org/10.1016/j.ijheatfluidflow.2024.109412.

Li, Y., Zhu, C., Fan, C., Zhang, T., Tian, H., Zeng, Y.J., Guo, W., 2026. Large-scale 3D experimental study on in-situ pyrolysis of tar-rich coal (I): heat transfer behavior and product characteristics under conductive heating. Pet. Sci. https://doi.org/10.1016/j.petsci.2026.04.003.

Li, Y., Zhu, C., Zeng, Y., Shui, H., Fan, C., Guo, W., 2023. Numerical simulations of the effects of bedding planes on hydraulic fracture propagation law in oil shale. Coal Geol. Explor. 51 (11), 44–54. https://doi.org/10.12363/issn.1001-1986.23.07.0397.

Liu, H., Zhu, H., Yan, L., Huang, Y., Kato, S., Kojima, T., 2011. Gasification reactivity of char with CO2 at elevated temperatures: the effect of heating rate during pyrolysis. Asia Pac. J. Chem. Eng. 6, 905–911. https://doi.org/10.1002/apj.483.

Liu, X., Liu, X., Hu, Y., 2015. Investigation of the thermal behaviour and decomposition kinetics of kaolinite. Clay Miner. 50 (2), 199–209. https://doi.org/10.1180/claymin.2015.050.2.04.

Lu, P., Wu, R., Xu, G., Wang, G., 2024. Influencing factors and identifying precursors in phenolic compounds formation from tobacco extracts pyrolysis. J. Anal. Appl. Pyrolysis 180, 106549. https://doi.org/10.1016/j.jaap.2024.106549.

Maloney, D.J., Sampath, R., Zondlo, J.W., 1999. Heat capacity and thermal conductivity considerations for coal particles during the early stages of rapid heating. Combust. Flame 116 (1), 94–104. https://doi.org/10.1016/S0010-2180(98)00044-3.

Qu, B.L., Zhu, H.Q., Wang, J.X., Li, B.R., Xie, L.H., Liao, Q., Hu, L.T., 2024. Dynamic evolution of terahertz permittivity of lignite during oxidation: microstructural insights. Appl. Energy 363, 123105. https://doi.org/10.1016/j.apenergy.2024.123105.

Renka, R.J., Renka, R., Cline, A., 1984. A triangle-based C^1 interpolation method. Rocky Mt. J. Math. 14 (1), 223–238. https://doi.org/10.1216/RMJ-1984-14-1-223.

Shamsi, A., Jafari, A., Gharibshahi, R., 2021. Nanoparticles assisted microwave radiation: fluid-rock interactions in oil reservoirs. Pet. Sci. 18 (6), 1797–1812. https://doi.org/10.1016/j.petsci.2021.09.002.

Shui, H., Liu, S., Liu, Z., Zhang, K., Li, L., Zhao, K., 2026. The parameters and applicability analysis of low calorific value gases applied to oil shale in situ conversion catalytic combustion heaters. ACS Omega 11 (19), 27838–27849. https://doi.org/10.1021/acsomega.5c10809.

Shui, H., Wang, Y., Li, Q., Fan, C., Li, Y., Zeng, Y., Guo, W., 2024. Analysis of heat transfer performance and system energy efficiency of catalytic combustion heaters for low calorific value waste gas application to oil shale in-situ conversion. Energy 294, 130690. https://doi.org/10.1016/j.energy.2024.130690.

Smart, J.P., O'Nions, P., Riley, G.S., 2010. Radiation and convective heat transfer, and burnout in oxy-coal combustion. Fuel 89 (9), 2468–2476. https://doi.org/10.1016/j.fuel.2010.03.048.

Suo, Y., Dong, M., Fu, X., He, W., Pan, Z., 2024a. Experimental and numerical simulation research on hot dry rock wellbore stability under different cooling methods. Geothermics 119, 102977. https://doi.org/10.1016/j.geothermics.2024.102977.

Suo, Y., Li, Z., Fu, X., Zhang, C., Jia, Z., Peng, D., He, W., Pan, Z., 2024b. Comprehensive study of hydraulic fracturing in shale oil reservoirs comprising shale–sandstone transitions. Phys. Fluids 36, 077161. https://doi.org/10.1063/5.0212983.

Tian, B., Qiao, Y., Tian, Y., Liu, Q., 2016. Investigation on the effect of particle size and heating rate on pyrolysis characteristics of a bituminous coal by TG–FTIR. J. Anal. Appl. Pyrolysis 121, 376–386. https://doi.org/10.1016/j.jaap.2016.08.020.

Tian, H., Guo, W., Li, Q., Deng, S., Bai, F., Li, Y., Zeng, Y., Zhu, C., 2025. High-pressure pyrolysis mechanism of tar-rich coal in Taiyuan Formation, Ordos Basin. Energy 337, 138675. https://doi.org/10.1016/j.energy.2025.138675.

Wang, C., Chang, Z., Ma, Y., Wang, C., Huang, H., Wang, X., Liu, S., 2025. Enhancing light tar production from tar-rich coal through low-temperature oxidation-assisted pyrolysis. J. Anal. Appl. Pyrolysis 191, 107232. https://doi.org/10.1016/j.jaap.2025.107232.

Wang, C., Wu, M., Mao, Q., Ning, X., Hou, Y., Yuan, T., Zhao, L., Yang, F., Ma, L., Duan, Z., 2024. Effects of physical property dynamic change on heat transfer characteristics of coal seam during in-situ pyrolysis of tar-rich coal. Numer. Heat Tran. 87 (1), 1–24. https://doi.org/10.1080/10407782.2024.2384617.

Wang, J., Xiao, L., Li, P., Arbuzov, S., Ding, S., 2019. Occurrence mode of selected elements of coal in the Ordos Basin. Energy Explor. Exploit. 37 (6), 1680–1693. https://doi.org/10.1177/0144598718763939.

Wang, L., Li, X., Chen, Y., Zhan, H., Pei, X., Chen, Y., Qi, N., He, W., Yu, W., Lin, Y., Zhou, Y., 2025. Reservoir heterogeneity in deep marine-continental transitional shales: the role of lithofacies and quality in the coal-bearing longtan formation, central Sichuan basin. Front. Earth Sci. 13, 1650521. https://doi.org/10.3389/feart.2025.1650521.

Wang, L., Yang, D., Kang, Z., 2021. Evolution of permeability and mesostructure of oil shale exposed to high-temperature water vapor. Fuel 290, 119786. https://doi.org/10.1016/j.fuel.2020.119786.

Wang, L., Yang, D., Zhang, Y., Li, W., Kang, Z., Zhao, Y., 2022. Research on the reaction mechanism and modification distance of oil shale during high-temperature water vapor pyrolysis. Energy 261, 125213. https://doi.org/10.1016/j.energy.2022.125213.

Wang, Z., Wang, Z., Wang, T., 2024. Research progress on heat effects of coal pyrolysis process. J. Anal. Appl. Pyrolysis 183, 106827. https://doi.org/10.1016/j.jaap.2024.106827.

Xu, S., Lü, X., Sun, Y., Guo, W., Li, Q., Liu, L., Kang, S., Deng, S., 2023a. Optimization of temperature parameters for the autothermic pyrolysis in-situ conversion process of oil shale. Energy 264, 126309. https://doi.org/10.1016/j.energy.2022.126309.

Xu, S., Lü, X., Wang, H., Sun, Y., Kang, S., Wang, Z., Guo, W., Deng, S., 2024. Characterization of oxygen initiation process in the autothermic pyrolysis in-situ conversion of Huadian oil shale. Pet. Sci. 21 (6), 4481–4496. https://doi.org/10.1016/j.petsci.2024.07.024.

Xu, S., Sun, Y., Lü, X., Yang, Q., Li, Q., Wang, Z., Guo, M., 2021. Effects of composition and pore evolution on thermophysical properties of Huadian oil shale in retorting and oxidizing pyrolysis. Fuel 305, 121565. https://doi.org/10.1016/j.fuel.2021.121565.

Xu, S., Sun, Y., Yang, Q., Wang, H., Kang, S., Guo, W., Shan, X., He, W., 2023b. Product migration and regional reaction characteristics in the autothermic pyrolysis in-situ conversion process of low-permeability Huadian oil shale core. Energy 283, 128525. https://doi.org/10.1016/j.energy.2023.128525.

Xu, S., Zeng, X., Han, Z., Cheng, J., Wu, R., Chen, Z., Masěk, O., Fan, X., Xu, G., 2019. Quick pyrolysis of a massive coal sample via rapid infrared heating. Appl. Energy 242, 732–740. https://doi.org/10.1016/j.apenergy.2019.03.079.

Yang, D., Wang, L., Zhao, Y., Kang, Z., 2021. Investigating pilot test of oil shale pyrolysis and oil and gas upgrading by water vapor injection. J. Pet. Sci. Eng. 196, 108101. https://doi.org/10.1016/j.petrol.2020.108101.

Yang, Q., Guo, W., Xu, S., Zhu, C., 2023. The autothermic pyrolysis in-situ conversion process for oil shale recovery: effect of gas injection parameters. Energy 283, 129134. https://doi.org/10.1016/j.energy.2023.129134.

Zhang, H., Bai, J., Kong, L., Dai, X., Bai, Z., Li, W., 2016. Thermal transformation of tobelite from coal at high temperatures and the kinetics and mechanism of dehydroxylation and deamination process. Fuel Process. Technol. 144, 203–211. https://doi.org/10.1016/j.fuproc.2015.12.021.

Zhang, X., Guo, W., Pan, J., Zhu, C., Deng, S., 2024. In-situ pyrolysis of oil shale in pressured semi-closed system: insights into products characteristics and pyrolysis mechanism. Energy 286, 129608. https://doi.org/10.1016/j.energy.2023.129608.

Zhao, J., Yang, D., Kang, Z., Feng, Z., 2012. A micro-CT study of changes in the internal structure of Daqing and Yan'an oil shales at high temperatures. Oil Shale 29, 357–367. https://doi.org/10.3176/oil.2012.4.06.

Zhao, S., Lü, X., Li, Q., Sun, Y., 2020. Thermal-fluid coupling analysis of oil shale pyrolysis and displacement by heat-carrying supercritical carbon dioxide. Chem. Eng. J. 394, 125037. https://doi.org/10.1016/j.cej.2020.125037.

Zhu, B., Guo, W., Sun, Y., Deng, S., Zhu, C., Liu, H., Li, Q., 2026. Field experiment study of well-group control and exploitation in Fuyu oil shale using topochemical heat in-situ conversion technology. Fuel 416, 138562. https://doi.org/10.1016/j.fuel.2026.138562.

Zhu, B., Guo, W., Sun, Y., Deng, S., Zhu, C., Wang, Y., Li, Q., 2025a. In-Situ field experiment study of thermal expansion and asphaltene blockage effects in Fuyu oil shale. Energy Fuels 39, 1166–1180. https://doi.org/10.1021/acs.energyfuels.4c05266.

Zhu, C., Guo, W., Sun, Y., Li, Q., Deng, S., Wang, Y., Cui, G., 2022. Reaction mechanism and reservoir simulation study of the high-temperature nitrogen injection in-situ oil shale process: a case study in Songliao Basin, China. Fuel 316, 123164. https://doi.org/10.1016/j.fuel.2022.123164.

Zhu, C., Zhang, T., Pan, J., Li, Y., Sheng, J.J., Ge, D., Jia, R., Guo, W., 2025b. Evolution of the 3D pore structure of organic-rich shale with temperature based on micro-nano CT. Pet. Sci. 22 (6), 2339–2352. https://doi.org/10.1016/j.petsci.2025.03.037.